University of Alberta

Neon in Porous Glass Samples and Aerogels

by

Hong Wee Tan

A thesis submitted to the Faculty of Graduate Studies and Research in partial fulfilment of the requirements for the degree of Master of Science

in

Department of Physics

Edmonton, Alberta

Fall, 1998

National Library of Canada
Acquisitions and Bibliographic Services
395 Wellington Street
Ottawa ON K1A 0N4
Canada

Bibliothèque nationale du Canada
Acquisitions et services bibliographiques
395, rue Wellington
Ottawa ON K1A 0N4
Canada

Your file Votre référence

Our file Notre référence

The author has granted a non-exclusive licence allowing the National Library of Canada to reproduce, loan, distribute or sell copies of this thesis in microform, paper or electronic formats.

The author retains ownership of the copyright in this thesis. Neither the thesis nor substantial extracts from it may be printed or otherwise reproduced without the author's permission.

L'auteur a accordé une licence non exclusive permettant à la Bibliothèque nationale du Canada de reproduire, prêter, distribuer ou vendre des copies de cette thèse sous la forme de microfiche/film, de reproduction sur papier ou sur format électronique.

L'auteur conserve la propriété du droit d'auteur qui protège cette thèse. Ni la thèse ni des extraits substantiels de celle-ci ne doivent être imprimés ou autrement reproduits sans son autorisation.

0-612-34425-8

Canada

University of Alberta

Library Release Form

Name of Author: Hong Wee Tan

Title of Thesis: Neon in Porous Glass Samples and Aerogels

Degree: Master of Science

Year this Degre Granted: 1998

Permission is hereby granted to the University of Alberta Library to reproduce single copies of this thesis to lend or sell such copies for private, scholarly, or scientific research purposes only.

The author reserves all other publication and other rights in association with the copyright in the thesis, and except as hereinbefore provided, neither the thesis nor any substantial portion thereof may be printed or otherwise reproduced in any material form whatever without the author's prior written permission

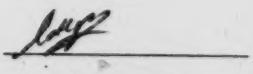

Hong Wee Tan
Blk 86, #09-592
Redhill Close
Singapore 150086

Date: 29-Jul-98

University of Alberta

Faculty of Graduate Studies and Research

The undersigned certify that they have read, and recommend to the Faculty of Graduate Studies and Research for acceptance, a thesis entitled Neon in Porous Glass Samples and Aerogels submitted by Hong Wee Tan in partial fulfilment of the requirements for the degree of Master of Science.

John Beamish

Dr. J. R. Beamish (Supervisor)

Frank Marsiglio

Dr. F. Marsiglio

J.-P. Franck

Dr. J. P. Franck

B. M. Patchett

Dr. B. Patchett

Date: July 28, 1998

ABSTRACT

Ultrasonic techniques were used to study the critical behavior of neon in bulk and in 95% porosity aerogels. For the former case, sharp cusps in the velocity and attenuation of the ultrasound signals were detected in the SH and L modes and believed to be indicators of phase transitions. Unusual patterns in the velocity curves were observed when near-critical neon was confined in the aerogel pores. The attenuation readings however revealed the usual sharp peaks. By using those dips and peaks as markers, both the coexistence curves of neon in bulk and in aerogels were sketched and compared. The curve for the aerogel-confined neon was only slightly narrower than that of the bulk. In addition, the confined curve was seen displaced towards the higher density edge with respect to that for the bulk. Compared to its bulk value, the critical temperature of the aerogel-confined neon was also moderately suppressed.

DEDICATION

To my beloved grandma

ACKNOWLEDGEMENTS

I will never be able to thank my supervisor, John Beamish, enough for his infinite support and advice throughout this research; without him, this project would not have been possible. A zillion thanks to Don Mullin for helping me with all those frustrating technical problems I faced and also to Yolande Peske and Steve Rogers for getting me that precious element, neon. Last but not least, I will like to express my appreciation to Lynn Chandler for the patience she demonstrated when I first came to this department and for all the administrative assistance she gave during my stay.

TABLE OF CONTENTS

Chapter		Page
1	**Basic Understanding**	1
	1.1 Introduction	1
	1.2 Aerogel Structure	2
	1.3 Ultrasound in Bulk Fluids	3
	1.4 Capillary Condensation and Hysteresis	5
	1.5 Critical Behavior of Fluids in Porous Materials	10
	1.5.1 Universality Classes	10
	1.5.2 Experimental Results	11
	1.5.3 Theoretical Modeling	12
	1.6 Ultrasound in Fluid Filled Porous Materials	17
2	**Experimental Setup**	22
	2.1 Properties of Glass Capillary Array Samples and Aerogels	22
	2.2 Sample Preparation	24
	2.3 Cryogenics and Thermometry	26
	2.3.1 Refrigerator	26
	2.3.2 Experimental Cell	28
	2.3.3 Thermometry	29
	2.4 Gas Delivery System	29
	2.5 Determination of Gas Density	30
	2.6 Ultrasonics	32
	2.7 Determination of Surface Area	35

3 Results and Analysis 37

3.1 Surface Area Determination 37

3.2 Properties of Near-Critical Neon 38

3.3 Ultrasound in Bulk Neon Confined in GCA Channels 39

3.4 Ultrasound in Neon Confined in Aerogels in GCA Channels 48

3.5 Coexistence Curves of Bulk and Confined Neon 53

3.6 Concluding Remarks 56

References 57

Appendix 59

LIST OF FIGURES

1.1	The phase diagram of helium in bulk and Vycor glass	1
1.2	Schematic drawing of the structure of silica aerogel	3
1.3	Sound velocity vs. temperature in xenon at 250, 750 and 1250 kHz	4
1.4	Attenuation vs. temperature in xenon at 250 kHz	4
1.5	Different types of hysteretic capillary condensation	5
1.6	Relation between r_m and r_p	7
1.7	Liquid-vapor coexistence curve of ^{4}He in aerogel	11
1.8	The mean-field coexistence curve of a periodic model with 96% porosity	16
1.9	Setting up the coordinate system	17
2.1	Edge of GCA sample seen under a scanning electron microscope	22
2.2	Thermodynamic path taken during the production of aerogel	26
2.3	Simplified diagram of the refrigerator	27
2.4	The experimental cell	28
2.5	The gas delivery system	29
2.6	Determination of total amount of gas in the system	31
2.7	Relationship between density of neon and filling pressure at 48 K	31
2.8	Schematic of the ultrasonic system	32
3.1	Adsorption isotherm of neon at 27 K	37
3.2	BET plot for neon confined in aerogel-filled GCA sample	37
3.3	Sound velocity change in the SH mode in bulk neon	40
3.4	Attenuation in the SH mode were propagated in bulk neon	41
3.5	Sound velocity change in the SH, L and SV modes in bulk neon	42
3.6	Attenuation in the SH, L and SV modes in bulk neon	43
3.7	Sound velocity change in the SH mode in neon confined within aerogel	49
3.8	Attenuation in the SH mode in neon confined within aerogel	50
3.9	Sound velocity change in the L mode in neon confined within aerogel	51

3.10 Attenuation in the L mode in neon confined within aerogel 52
3.11 Coexistence Curves of Bulk Neon and Neon Confined in 95% Aerogel 54
3.12 Fitting the Coexistence Curve of Bulk Neon 54

Chapter 1: Basic Understanding

1.1 Introduction

When pure liquids or binary liquid mixtures are confined in porous media such as Vycor glasses and silica gels, their phase behavior may sometimes be altered drastically. Using heat capacity and ultrasonic measurements, the freezing transitions of several liquids such as hydrogen, neon, argon and oxygen in porous media were found [1.1] to be markedly different from that in the bulk. The temperature which marked the onset of solidification was depressed and the process itself appeared continuous over a finite temperature range. Chan *et al.* showed that the vapor-liquid coexistence curves of helium-4 [1.2] and nitrogen [1.3] were shifted to lower temperatures and higher densities when confined in silica gels. Similar results were also obtained for the phase separation of isobutyric acid-water mixtures by Zhuang *et al.* [1.4]. Other phenomena include the displacements of the superfluid transition curves of confined ^{4}He [1.5] and ^{4}He-^{3}He mixtures [1.6] from those of the bulk.

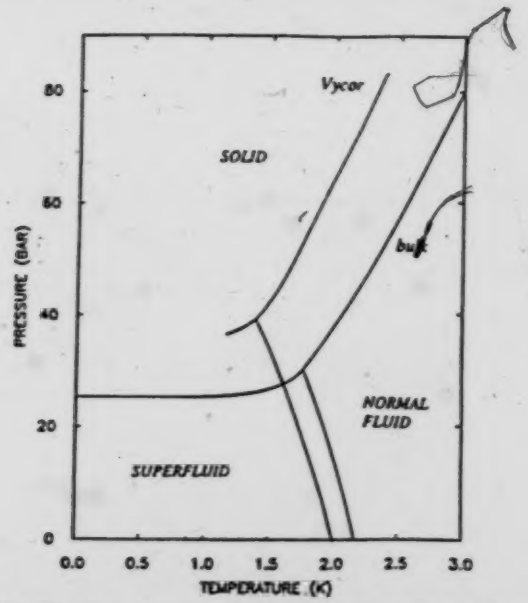

Fig. 1.1 The phase diagram of helium in bulk and Vycor glass

In all these experiments, the porous samples used usually occupied only a few percent of the total volume. Therefore, to find such pronounced changes in phase transitions and critical behavior due to so little amounts of quenched, i.e. spatially fixed, impurities in the form of dilute gel is truly an amazing discovery.

For this work, the effects neon confinement in aerogel (contained in porous glass samples) have on critical behavior will be studied using ultrasonic techniques. Such techniques which involve the measuring of changes in sound speeds and attenuation have often been employed to provide a sensitive means of detecting phase transitions. By virtue of its simple nature and relatively high critical point (cf. helium), neon is considered an experimentally convenient choice for this work.

1.2 Aerogel Structure

Aerogels are highly porous materials made from the development of a polymer network in a chemical solution followed by hypercritical drying. The properties of these materials depend strongly on the preparation procedure, e.g. the pH value of the starting solution, aging time and baking time. Structurally, silica aerogels consist of small silica spheres, usually 2 to 10 nm in diameter, which cluster to form interconnected branched strands. The spaces between these strands range from 1 to 100 nm. Depending on the amount of methanol used during the preparation stage, aerogels can be made with porosities ranging from 85 to over 99%. Their surface areas can sometimes be as large as 1000 m^2/g.

Aerogels form volume fractals whose mass within a scale L has a power law dependence of $M \propto L^d$ whereby d is normally a non-integral number smaller than 3. These fractal structures appear over a range of length scales from about 1 to 30 nm and they are self-similar, that is to say, they look the same at any magnification.

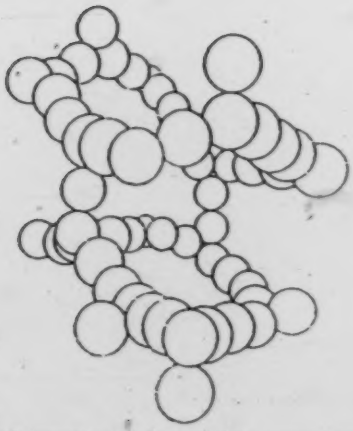

Fig. 1.2 Schematic drawing of silica aerogel structure

1.3 Ultrasound in Bulk Fluids

Under adiabatic conditions whereby there is insufficient time for thermal conduction to occur between the local disturbances set up by the transmitted signals and the surroundings, the real part of the complex sound velocity in a medium can be written as

$$u = \frac{1}{\sqrt{\rho \kappa_s}} \tag{1.1}$$

Here, ρ and κ_s are the mass density and adiabatic compressibility of the medium respectively. However, near the critical point, the isothermal compressibility κ_T of the medium is expected to have an infinite singularity since $(\partial p/\partial \rho)_{TC}=0$. From the thermodynamic relationship

$$\frac{1}{\kappa_s} = \frac{1}{\kappa_T} + \frac{T}{\rho C_v}\left(\frac{\partial p}{\partial T}\right)_v^2 \tag{1.2}$$

one then obtains

$$\rho u^2 \approx \frac{T}{\rho C_v}\left(\frac{\partial p}{\partial T}\right)_v^2 \text{ as } T \to T_C \tag{1.3}$$

The critical behavior of u^2 is thus predicted to be similar to that of C_V^{-1} since the other quantities in eq. (1.3) are either constant or slowly varying. In fact, ultrasound velocity in a medium displays a sharp cusp near the critical temperature, not unlike the critical behavior of C_V whose variation with temperature may be expressed as

$$C_v \sim |t|^{-\alpha} \qquad (1.4)$$

Here, $t=(T-T_c)/T_c$ is the reduced temperature and α, the critical exponent, has a value of about 0.11.

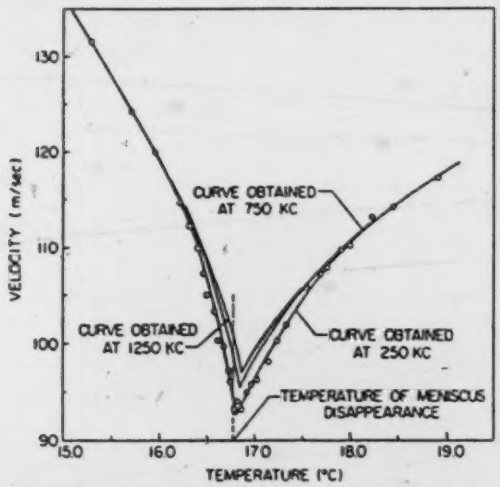

Fig. 1.3 Sound velocity vs. temperature in xenon at 250, 750 and 1250 kHz

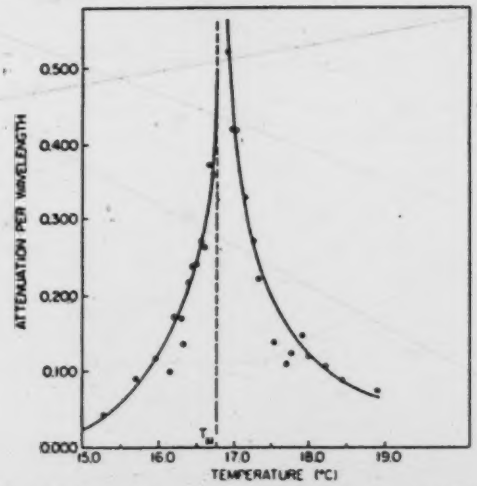

Fig. 1.4 Attenuation vs. temperature in xenon at 250 kHz

It is also known that ultrasonic attenuation increases dramatically near the critical point. A sound wave sets up pressure and temperature gradients within a medium so that small scale flows of matter and energy result. These dissipative processes give rise to attenuation. However, near the critical point, Chynoweth and Schneider [1.7] proposed that large clusters of fluid (involving perhaps 10^9 molecules or more) having densities momentarily very different from that of their surrounding are formed. These clusters display a spectrum of lifetimes which tends to shift towards longer times and to become even broader as the critical point is approached. As a result, the accompanying attenuation increases dramatically. In fact, Kawasaki [1.8] claimed that the critical behavior of attenuation may be deduced from the fluid's frequency-dependent viscosity alone. In any case, relaxation processes are believed to be the physical mechanisms responsible for the very large attenuation observed in fluids near their critical points.

1.4 Capillary Condensation and Hysteresis

Hysteretic capillary condensation is commonly observed during the adsorption and desorption of a fluid in a porous sample.

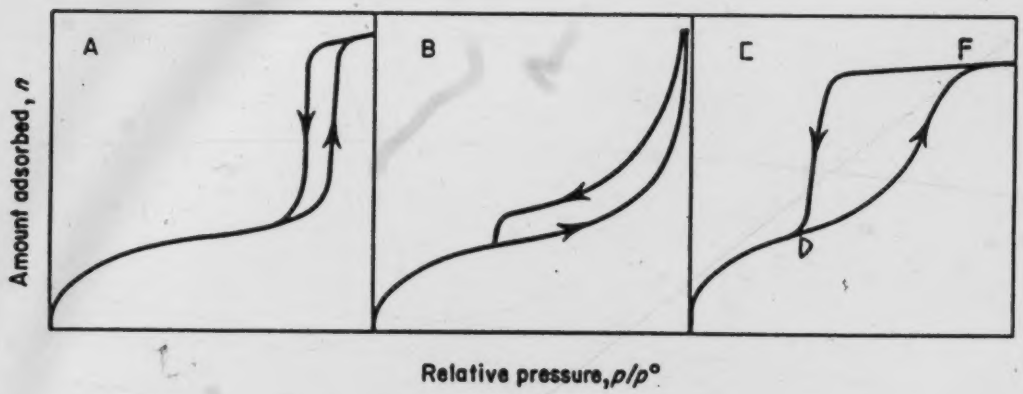

Fig. 1.5 Different types of hysteretic capillary condensation

This well known phenomenon can be explained to some extent by the classical Kelvin equation. Suppose a pure liquid (l) confined within a cylinder of radius r_p is in equilibrium with its vapor (g). The condition for mechanical equilibrium is given by the Young-Laplace equation

$$P^g - P^l = \frac{2\gamma}{r_m} \tag{1.5}$$

where P, r_m and γ are the pressure, mean curvature radius of the liquid-vapor interface and surface tension respectively. Here, it is assumed that the center of curvature lies in the vapor i.e. the meniscus is concave. The condition for thermodynamic equilibrium on the other hand is given by

$$\mu^g = \mu^l \tag{1.6}$$

where μ is the chemical potential. If we now pass from one equilibrium state to another at constant temperature, then eq. (1.5) and (1.6) respectively become

$$dP^g - dP^l = d(\frac{2\gamma}{r_m}) \tag{1.7}$$

$$d\mu^g = d\mu^l \tag{1.8}$$

Each phase must also satisfy a Gibbs-Duhem equation, so that

$$s^l dT + v^l dP^l + d\mu^l = 0 \tag{1.9}$$

$$s^g dT + v^g dP^g + d\mu^g = 0 \tag{1.10}$$

where s and v are the molar entropy and volume respectively.

At constant temperature, combining eq. (1.7) to (1.10) leads to the relation

$$(\frac{v^l - v^g}{v^l})dP^g = d(\frac{2\gamma}{r_m}) \qquad (1.11)$$

Since $v^l << v^g$ and if the vapor behaves as an ideal gas, then one obtains

$$\frac{RT}{v^l}d(\ln P^g) = -d(\frac{2\gamma}{r_m}) \qquad (1.12)$$

Upon integration between the limits (r_m, P) and (∞, P_o), this becomes

$$\ln\frac{P}{P_o} = -\frac{2\gamma v^l}{RT}\frac{1}{r_m} \qquad (1.13)$$

where P_o is the saturation vapor pressure. The tacit assumption made during integration is that the liquid volume v^l is independent of pressure, i.e. the liquid is incompressible.

Suppose the cylindrical pore is open at both ends. During adsorption, the pore walls are covered with a very thin film of liquid and consequently, the meniscus is cylindrical in form. It can then be argued geometrically that the mean radius of curvature is given by $r_m=2r_p$. Conversely, during desorption, the pores are full of liquid and evaporation takes place from the meniscus at either end so that $r_p=r_m\cos\theta$ where θ is the angle of contact between the liquid and capillary walls.

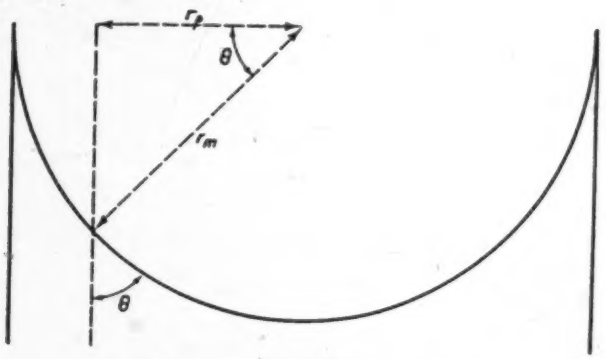

Fig. 1.6 Relation between r_m and r_p

With these in mind, the complete Kelvin equations are then written as

$$\ln(\frac{P}{P_o}) = -\frac{\gamma v^l}{RT}\frac{1}{r_p} \text{ for adsorption} \qquad (1.14)$$

$$\text{and} \quad \ln(\frac{P}{P_o}) = -\frac{\gamma v^l}{RT}\frac{2}{r_p}\cos\theta \text{ for desorption} \qquad (1.15)$$

Fig. 1.5(c) can now be explained as follows. During the initial stage of the isothermal process, adsorption is restricted to a thin layer on the walls until the pressure at D is reached. At this point, capillary condensation commences in the finest pores. As the pressure is increased progressively, wider pores become filled until the system is full at point F. At all times, capillary condensation occurs at pressure values lower than the saturation vapor pressure of the bulk fluid, provided the meniscus is concave. The same explanation applies for desorption, only this time, the pressure needed for evaporation is lower than that for condensation. The origin of hysteresis lies in the different radii of curvature of the liquid-vapor interface during adsorption and desorption. If the pore size distribution narrows, the hysteretic region sharpens and fig. 1.5(a) is obtained.

There are however many criticisms against this classical theory. For example, the Kelvin equation completely omits the van der Waals forces between liquid films and pore walls. These forces are believed to dominate the physics of thin films. Also, the Kelvin equation is no longer applicable once the fluid starts to exhibit critical behavior since the liquid phase is highly compressible in that regime.

In another theory proposed by Cole and Saam [1.9], the entire process of capillary condensation is described in terms of the excitation spectrum of thin films and the thermodynamics of adsorption. Basically, two kinds of oscillatory motion in thin films are considered: one localized near the liquid-vapor interface and another involving the propagation of phonons through the liquid. In both cases, the motion is affected by boundary conditions at the vapor and substrate interfaces with the liquid. It must be pointed out that although this theory was originally developed for liquid helium films, its general results had been found to hold for other systems as well [1.10].

During the filling process, the layer of adsorbed film gradually thickens until it becomes energetically favorable to partially fill the pore in order to reduce the surface area. By taking into account the factors mentioned above, a certain radius of instability a_c can be determined. In terms of the scaling parameter R_o, where $R_o=(3\pi\alpha\rho/\gamma M)^{1/2}$, this instability criterion can be expressed in dimensionless units as

$$(\frac{r_p}{R_o})^2 = y_c^2 (1 - y_c^2)^{-5/2} P^1_{3/2}\left[\frac{1+y_c^2}{1-y_c^2}\right] \qquad (1.16)$$

Here α is the gas-substrate van der Waals interaction coefficient, ρ the liquid density, γ the surface tension, M the molecular weight, r_p the pore radius, $y_c=a_c/r_p$ and $P^1_{3/2}$ an associated Legendre function. Similarly, during the emptying process, there exists a certain radius a_v at which the film is metastable relative to the partially filled pore so that it becomes energetically favorable for the system to assume a layered configuration. This radius has been worked out as

$$2a_v^{-2} \int_0^{a_v} r\,U(r)\,dr = U(a_v) + \frac{\sigma M}{a_v \rho} \qquad (1.17)$$

where U(r) is the gas-substrate van der Waals interaction potential. When this theory was tested by Awschalom *et al.* [1.10] in their study on the adsorption and desorption of oxygen in aerogel samples, it was proven to be far superior to the classical explanation.

Without going into details about pore structures or liquid menisci shapes, this new proposal is able to give surprisingly accurate accounts of hysteretic behavior.

1.5 Critical Behavior of Fluids in Porous Materials

1.5.1 Universality Classes

In near-critical fluids, the correlation between two atoms separated by distance r decays as $e^{-r/\xi}$ where ξ is a characteristic correlation length. The latter diverges as

$$\xi = \xi_o |t|^{-\nu} \qquad (1.18)$$

where ξ_o is the two-phase correlation length amplitude and ν, the critical exponent, is approximately 0.63. Since the correlation length becomes very large compared to typical interatomic spacings near the critical point, many microscopic details may be deemed unimportant for studies on critical behavior. It follows then that such systems can be divided into broad groups known as universality classes such that all members of a given class have 'identical' critical properties. For example, near-critical simple liquids, binary liquid mixtures and the three dimensional Ising model (later, sec. 1.5.3) belong to the same universality class.

In the case of simple liquids, if the average of the liquid and vapor densities below the critical temperature T_c is the critical density (i.e., $\rho_L+\rho_v=2\rho_c$), then the order parameter which in this case is the density difference between the two phases, may be described by

$$\Delta\rho = B|t|^{\beta} \qquad (1.19)$$

Here, $\Delta\rho=(\rho_l-\rho_v)/2\rho_c$, β and B are the reduced density, critical exponent and amplitude fit respectively. The value of B simply characterizes the width of the coexistence curve and β is theoretically predicted to be 0.325 [1.11]. It must however be pointed out that this simple power law is valid only in regions sufficiently close to the critical region. Whether this universality class of liquid-vapor transitions and phase-separations remains the same when the systems are confined in porous media is still a topic under intense study at the moment.

1.5.2 Experimental Results

Chan *et al.* [1.2] found through heat capacity measurements that the liquid-vapor coexistence curve of helium-4 (^{4}He) was made narrower by 14 times when it was confined in 95% porosity aerogel. In addition, the critical temperature and density of bulk ^{4}He were also observed to be shifted by -0.031 K and 0.0112 g/cm^3 respectively.

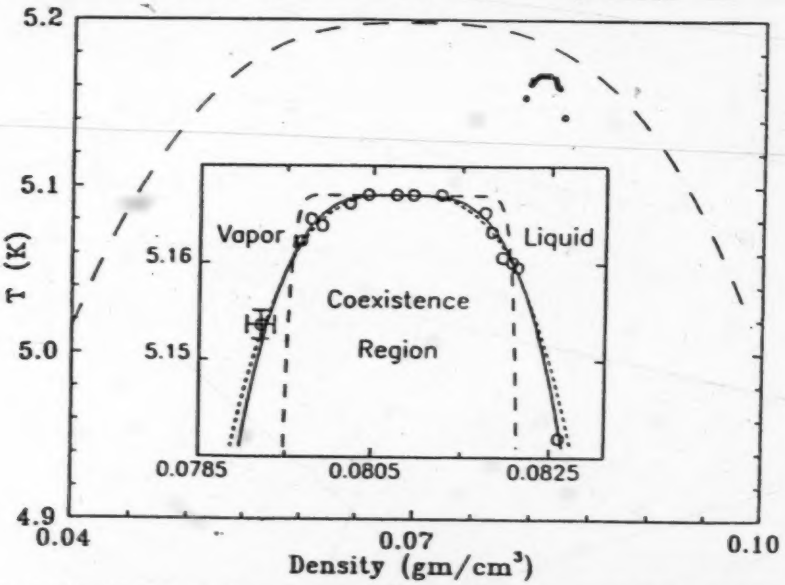

Fig. 1.7 Liquid-vapor coexistence curves of ^{4}He in bulk and in aerogel. The dashed line is the bulk curve and the circles are data points obtained for the aerogel system. The inset magnifies the coexistence boundary in the aerogel. Within the inset, the solid, dotted and dashed lines show the best fit curves for β = 0.28, β = 0.325 (bulk value) and β = 0.05 (RFIM prediction; see sec. 1.5.3)

If eq. (1.19) is used to fit both the coexistence curves of the bulk and confined systems respectively, then the best fit parameters for the bulk system are ρ_c=0.0696 g/cm^3, T_C=5.198 K, β=0.355 and B=2.7909. For the aerogel system, these values are ρ_c=0.0808 g/cm^3, T_C=5.167 K, β=0.28 and B=0.200. The fact that both the measured values of β appear to be fairly close seems to suggest that the critical behavior of ^{4}He is still bulk-like despite its confinement in a random host.

In another experiment using light scattering techniques, similar findings were again reported by Chan *et al.* [1.3] when nitrogen (N_2) was confined in the same aerogel used previously. By utilizing the principle of enhanced scattering of light due to strong density fluctuations near each liquid-vapor transition temperature, i.e. critical opalescence, they were able to map out the coexistence curve of N_2 entrained in aerogel. In this case, the fitting parameters for bulk N_2 were found to be ρ_c=0.314 g/cm^3, T_C=126.2143 K, β=0.327 and B=2.958, but for N_2 in aerogel, they became ρ_c=0.33 g/cm^3, T_C=125.37 K, β=0.35 and B=1.183. Thus, when N_2 was confined in 95% aerogel, the change in the critical temperature and density were -0.84 K and 0.016 g/cm^3 respectively. Unlike ^{4}He, the width of the coexistence curve of this system was reduced by merely 2.5 times when it was confined in aerogel. However, similar to ^{4}He, the universality class of the N_2 liquid-vapor transition appeared to be the same for both the bulk and confined systems.

1.5.3 Theoretical Modeling

One model that has been applied fairly successfully to the experimental results of Chan *et al.* [1.2, 1.3] is the random-field Ising model (RFIM) [1.12]. For this work, however, the mean field treatment of a periodic model proposed by Donley and Liu [1.13] appears to be more applicable. So, only a brief description of the former model will be given here.

To describe the behavior of liquid-vapor systems in the presence of quenched impurities, RFIM introduces random fields h_i into a system of Ising spins s_i which can either point up (s_i=+1) or down (s_i=-1). The interactions of these spins with each other and with the random fields then correspond to the interactions of atoms with one another and with impurities introduced into the fluids. The resultant Hamilitonian of the system can be written as:

$$H = -(J/N) \sum_{i \neq j} s_i s_j - \sum_i h_i s_i \qquad (1.20)$$

where J>0 is the exchange interaction between two spins and N is the total number of spin sites. The probability distribution of the random fields is often given by

$$P(h_i) = p\delta(h_i - h_o) + (1-p)\delta(h_i + h_1) \qquad (1.21)$$

which indicates that a fraction p of the sites have a magnetic field h_o>0 whilst the rest of the sites have a field $-h_1$<0. Two fields of opposite signs are needed to create three possible ground states corresponding to all spins being +1, all spins being -1 and sites with h_o (h_1) being +1 (-1) respectively. In the current context, they are equivalent to the liquid phase, vapor phase, and vapor phase with a liquid layer coating the glass. Following this, the quenched free energy per site can be evaluated as

$$f = Jm^2 - (1/\beta)\{p \ln\cosh[\beta(2Jm + h_o)] + (1-p)\ln\cosh[\beta(2Jm - h_1)]\} \qquad (1.22)$$

where $\beta = 1/k_B T$. By using eq. (1.22), a three-dimensional (h_o-h_1-T) phase diagram can then be constructed. This model predicts that for any confined system, there exists a sharp critical temperature below which the system is unable to achieve equilibrium in any reasonable amount of time and will thus exhibit hysteretic behavior. In sec. 1.4, it was mentioned that hysteresis is believed to be a natural consequence of the interaction between confined fluids and the pore surfaces. Interestingly, the prediction made here is indirectly lending support to this notion since it is based on the interactions of spins with magnetic fields.

In addition, the coexistence region for any confined system is also expected to shrink together with a lowering of the transition temperature. This last prediction is certainly supported by most experimental observations.

In Donley and Liu's work, the model porous medium employed is a regular hexagonal array of infinitely long and thin cylinders of radius a, spaced at distance δ_x apart. The cylinders represent gel strands and the spaces between the strands are filled with a magnetization m(r). Because m(r) is spatially periodic and independent of z, the coordinate along the axial direction of the cylindrical strands, it is sufficient to only solve for m(r) in the two-dimensional hexagonal unit cell. In order to ensure continuity of the derivative of m(r), the normal derivative of the magnetization at the boundary of the unit cell is chosen as zero. Lastly, a Wigner-Seitz approximation is adopted so that the hexagonal unit cell is replaced by a circular one of the same area and whose radius b is related to δ_x, the distance between two strands, by

$$b = \frac{3^{1/4}}{\sqrt{2\pi}}\delta_x \qquad (1.23)$$

The total free energy of this system is given by:

$$\Omega(m) = \Omega_s(m_s) + \Omega_b(m) \qquad (1.24)$$

where Ω_s and Ω_b are the surface and bulk contributions respectively. m_s and m refer to spins on the surface and in the bulk respectively. These energy terms had been worked out previously by Nakanishi and Fisher [1.14] as:

$$\Omega_s(m_s) = -\frac{2\pi a}{\xi_{so}^2}[H_s m_s + \frac{1}{2}g m_s^2] \qquad (1.25)$$

$$\text{and} \quad \Omega_b(m) = 2\pi\int_a^b r\{f_B(m(r)) - Hm(r) + \frac{\kappa^2}{2}(\frac{dm}{dr})^2\}dr \qquad (1.26)$$

In eq. (1.25), H_s (> 0) and m_s are the surface field and magnetization on the strands respectively, and g is a surface parameter which accounts for the fact that spins on the surface have fewer neighbors than those in the bulk. As usual, ξ_o is the two-phase correlation length amplitude. In eq. (1.26), H (< 0) is a uniform bulk magnetic field and κ^{-1} is a bulk parameter related to the interaction range of the spins. Indeed, it is the interaction of the spins with the two competing fields, H in the bulk and H_s on the strand surfaces, which gives rise to differences in behavior between bulk systems and systems confined in porous mediums. $f_B(m)$ is the free energy density of a uniform system with average magnetization m and it may be expressed as:

$$f_B(m) \propto \tfrac{1}{2}tm^2 + \tfrac{1}{4}um^4 \qquad (1.27)$$

The coefficient u (> 0) merely sets the width of the coexistence curve of the bulk system. Minimizing eq. (1.24) yields a second order, nonlinear differential equation for m(r) which may be solved numerically. After computing the average magnetization (the equivalent of density in liquid-vapor systems)

$$< m >= 2\int_a^b m(r)\frac{r}{b^2-a^2}\,dr \qquad (1.28)$$

the relation between <m>, H and t can then be used to construct the final coexistence curve. By choosing the parameters as $H_s/k_BT=2$, $g/k_BT=-1$ and u=1, the coexistence curves for a simulated gel model with 96% porosity were obtained, as shown in fig. 1.8.

It can be seen that this model predicts a shift in the critical point towards higher magnetization (or equivalently, higher density) and lower temperature. Such shifts are almost always seen (see fig. 1.7) and are due to the competing interactions of the atoms with the gel surfaces and the rest of the bulk.

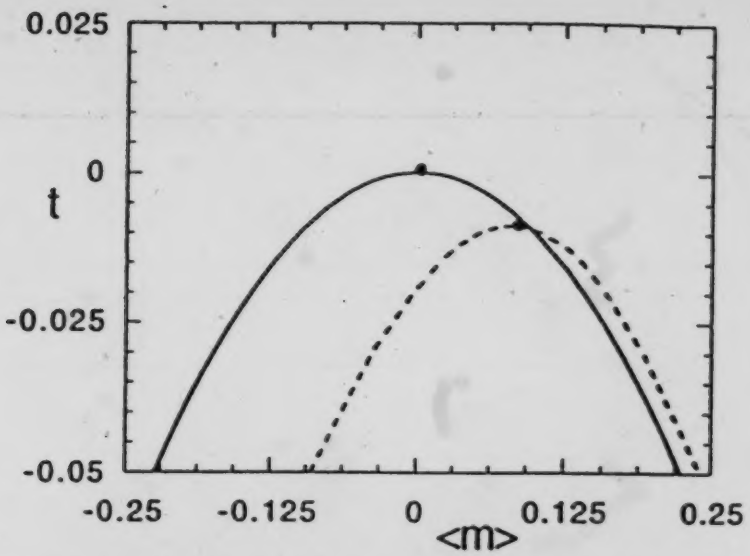

Fig. 1.8 The mean-field coexistence curve of a periodic model with 96% porosity
Solid line = curve for bulk and Dashed line = curve for gel system

Nevertheless, there are also some important differences between the results of this model and the experimental data of Chan *et al.* [1.2, 1.3]: firstly, in this model, the coexistence curve for the gel system is not expected to be much narrower than that for the bulk and secondly, the right edge of the coexistence curve for the model gel system falls outside that for the bulk (which, in our context, will mean the liquid phase in the gel system is denser than that in the bulk). However, if fluctuation effects are taken into account by using an interpolated linear model to obtain a different expression for the bulk free energy in eq. (1.27), both aforementioned differences may be reconciled. It is also believed that both long range surface interactions and the fractal nature of aerogels may lead to further narrowing of the coexistence curve for the gel system. In fact, when low values of H_1 (implying weak surface interactions) are used together with the interpolated linear model, the gel system yields a narrow coexistence curve that becomes a shoulder at low temperatures before it widens further. With even smaller values of H_1, a broad coexistence curve similar to the one shown in fig. 1.8 is obtained.

1.6 Ultrasound in Fluid Filled Porous Materials

Consider a solid sample with bulk density ρ_s having a fraction ϕ of its volume emptied so that after it is filled with parallel cylindrical pores of radius r_p, its effective density is given as

$$\rho_p = (1 - \phi)\rho_s \qquad (1.29)$$

If ultrasonic waves whose wavelength is much greater than the diameter of the pores is transmitted through the above sample, then any acoustic scattering associated with the pores is negligible and the sample can thus be treated as a homogenous medium.

Suppose the coordinate system shown in fig. 1.9 is set up such that the pore axes lie along the z direction and the direction of propagation of sound waves is in the x direction. For simplicity, we shall refer to longitudinal sounds whose polarization lies along the x-axis as the L mode. Similarly, shear sounds with polarizations along the y and z axes will be denoted as SH and SV modes respectively.

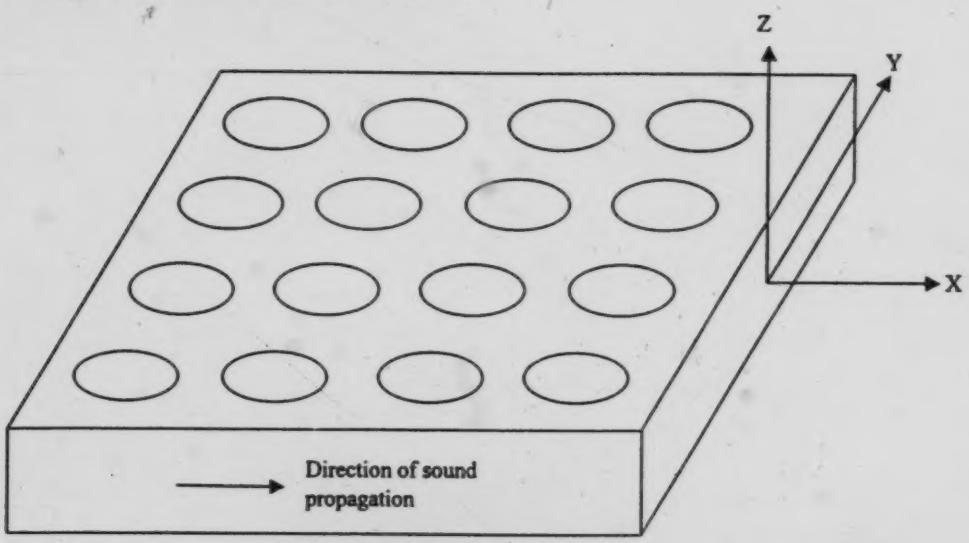

Fig. 1.9 Setting up the coordinate system

In an empty isotropic porous medium, the velocity of a shear wave is

$$v_s = \sqrt{\frac{\mu_p}{\rho_p}} \qquad (1.30)$$

and that of a longitudinal wave is

$$v_l = \sqrt{\frac{\kappa_p + 4/3\mu_p}{\rho_p}} \qquad (1.31)$$

Here, μ_p and κ_p are the shear and bulk modulus of the medium respectively. Typically, sound velocities decrease with increasing porosity since the shear and bulk modulus of porous materials tend to decrease faster with ϕ than density.

Now, suppose shear ultrasonic waves of angular frequency ω are transmitted through the above sample after it is filled with a fluid of viscosity η and density ρ_f. Since the characteristic relaxation time of most fluids is much shorter than an ultrasonic period, the fluid displays no rigidity and hence makes no contribution to the overall shear modulus. However, the fluid may contribute to the system density, depending on whether it oscillates together with the matrix.

In the SH mode, the fluid is always locked to the pore surfaces by inertial coupling (see fig. 1.9) so that the system's effective density becomes

$$\rho_e = \rho_p + \phi\rho_f \qquad (1.32)$$

One then obtains the resultant velocity of the shear waves as

$$v_{SH} = \sqrt{\frac{\mu_p}{\rho_e}} = \sqrt{\frac{\mu_p}{\rho_p + \phi\rho_f}} \qquad (1.33)$$

Since the fluid moves rigidly with the pores, there will not be any viscous attenuation.

However, in the SV mode, only a certain amount of fluid that is viscously coupled to the pore walls is dragged into motion by shear forces. The amplitude of oscillation in the fluid decreases with distance from the pore surfaces so that at a certain distance equal to the viscous penetration depth, given here as

$$\delta = \sqrt{\frac{2\eta}{\omega\rho_f}} \tag{1.34}$$

the amplitude is reduced by a factor of 1/e.

When the pore sizes are much smaller than the fluid's viscous penetration depth in the above case, the fluid is fully coupled to the pore surfaces. In this low frequency or high viscosity regime, the expression for the sound velocity (v_o) is the same as that given in eq. (1.33). According to Biot's theory [1.15], the viscous attenuation in the low frequency regime is of the form

$$\alpha|_{\omega\to 0} = \frac{K_o\omega^2}{2v_o\eta}\cdot\frac{\rho_f^2}{\rho_e} \tag{1.35}$$

Here, K_o is the sample's permeability and it relates fluid flow within the sample to the pressure gradient established. It is apparent from eq. (1.34) that if the viscous penetration depth of the fluid is decreased, say by increasing the frequency, there will be a corresponding increase in the motion of the fluid within the pores and larger attenuation effects due to viscosity are then obtained.

On the other hand, if the pore sizes are comparable to or larger than the fluid's viscous penetration depth, then the fluid is completely decoupled and makes no contribution to the overall density. In this high frequency or low viscosity regime, the sound velocity (v_∞) is the same as that given in eq. (1.30) and the viscous attenuation is

$$\alpha|_{\omega\to\infty} = \frac{\phi}{v_o\rho_e r_p}\cdot\sqrt{\frac{\eta\omega\rho_f}{1-\phi\rho_f/\rho_e}} \tag{1.36}$$

Such losses take place primarily in a thin layer on the pore surface.

For most porous materials such as aerogels, the pores are randomly oriented. In order to measure the degree of twistedness of the pores, a quantity known as tortuosity (τ) is introduced. The latter is also used to determine the fraction of fluid that is inertially coupled to the matrix. Thus, if a fraction $1/\tau$ of fluid decouples then the overall density of the system becomes

$$\rho_{eff} = \rho_p + (1 - \tfrac{1}{\tau})\phi\rho_f \qquad (1.37)$$

For the SV mode, τ is equal to 1 in the high frequency regime. But in the SH and L modes, τ tends to infinity. In the case of random orientation, an intermediate value of τ is obtained, and the resultant velocity and viscous attenuation for an isotropic medium in the high frequency regime are expressed respectively as

$$v_s|_{\omega\to\infty} = \sqrt{\frac{\mu_p}{\rho_p+(1-1/\tau)\phi\rho_f}} \qquad (1.38)$$

$$\alpha|_{\omega\to\infty} = \frac{\phi}{\tau v_o \rho_e r_p}\cdot\sqrt{\frac{\eta\omega\rho_f}{1-\phi\rho_f/\tau\rho_e}} \qquad (1.39)$$

Of course, in the low frequency regime, no decoupling takes place so the resultant velocity and attenuation are the same as that given in eq. (1.33) and (1.35) respectively.

In the L mode, the bulk modulus of the fluid (K_f) contributes to the resultant sound speed so that if the fluid is a lot more compressible than the matrix (K_{Si}, $K_p >> K_f$), then the respective velocities in the low and high frequency regimes are

$$v_l|_{\omega\to 0} = \sqrt{\frac{\kappa_p+\frac{4}{3}\mu_p+\frac{1}{\phi}(1-\kappa_p/\kappa_{Si})^2\kappa_f}{\rho_p+\phi\rho_f}} \qquad (1.40)$$

$$v_l|_{\omega\to\infty} = \sqrt{\frac{\kappa_p+\frac{4}{3}\mu_p+\frac{1}{\phi}(1-\kappa_p/\kappa_{Si})^2\kappa_f-\frac{1}{\tau}(2-\phi-\kappa_p/\kappa_{Si})\kappa_f}{\rho_p+(1-1/\tau)\phi\rho_f}} \qquad (1.41)$$

Like the SH mode, there is no viscous loss.

Chapter 2: Experimental Setup

2.1 Properties of Glass Capillary Array Samples and Aerogels

The glass capillary array (GCA) samples used in this work are provided by Collimated Holes Inc. Under suitable magnification, the capillary arrays appear to be made up of hexagonal bundles of regular cylindrical pores with 10 μm diameters.

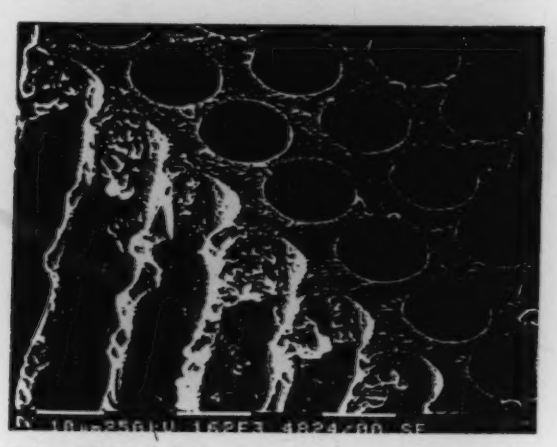

Fig. 2.1 Edge of GCA sample seen under a scanning electron microscope

To find the porosity ϕ and density ρ_p of each sample, three measurements were taken: the mass of the dry sample (M_D), the mass of the sample after it was completely saturated with water (M_w) and the apparent mass of the sample when it was submerged in water (M_s). For the last measurement, the water was boiled and cooled before it was used so that the formation of air bubbles could be prevented. If V is the volume of the sample, then these three masses may be expressed as $M_D=V\rho_p$, $M_w=V(\rho_p+\phi\rho_w)$ and $M_s = V(\rho_p+(\phi-1)\rho_w)$ where ρ_w is the density of water. Following this, the required quantities may be evaluated using the expressions

$$\phi = \frac{M_W - M_D}{M_W - M_S} \qquad (2.1)$$

$$\text{and} \quad \rho_P = \frac{M_D}{M_W - M_S}\rho_W \qquad (2.2)$$

The porosity and density of the GCA sample were thus found to be 53.0% and 1.29 g/cm^3 respectively. Next, by inserting the required values into eq. (1.29), the density of the non-porous glass was obtained as 2.74 g/cm^3. Since the external surface area of the samples was small compared to its total surface area, the specific area of the GCA samples could be estimated using

$$\frac{S}{M} = \frac{2\phi}{\rho_p r_p} \qquad (2.3)$$

as 0.183 m^2/g.

Because the GCA samples used in this work belong to the hexagonal system, all planes that contain the z-axis (also, the pore axis) are equivalent as far as elastic properties are concerned. Hence, velocities in the horizontal plane do not depend on the direction of propagation. At room temperature, the sound speeds for the L, SH and SV modes in the GCA samples were found to be 3300, 1500 and 2700 ± 100 m/s respectively. If the frequency of an applied signal is 10 MHz, then their respective wavelengths will be 330, 150 and 270 μm. Since these wavelengths are much greater than the size of the pores, the GCA samples may be treated as homogenous media.

Unlike isotropic aerogel samples, these glass samples possess 5 instead of just 2 elastic moduli (shear and bulk). Their relationships with the corresponding sound velocities are the same as that given in eq. (1.30). For a hexagonal system, the elastic moduli corresponding to the L, SH and SV modes are known as C_{11}, C_{66} and C_{44} [2.1] and in this case, their values may be worked out as 12×10^9, 3.4×10^9 and 7.8×10^9 N/m^2 respectively.

In this work, aerogels of 95% porosity were utilized. Using eq. (1.29) and the measurements of Ying [2.2], these aerogels will have an approximate density of 0.110 g/cm^3. In addition, the longitudinal and shear sound speeds in aerogels of density 0.254 g/cm^3 were also determined by the above author as 235 and 155 m/s respectively. Because sound speeds in aerogels (with density ρ greater than 0.1 g/cm^3) scale as $\rho^{1.3}$ [2.3], the relevant values in this case will then work out roughly as 80 and 50 m/s respectively. Such sound speeds will translate into wavelengths of 8 and 5 μm under an applied frequency of 10 MHz. As these wavelengths are much larger than typical pore sizes of aerogels (~ 0.1μm), the latter may also be treated as homogenous media.

2.2 Sample Preparation

To prepare usable GCA samples, smaller pieces were cut from the supplied ones with a string saw. After the ends were polished parallel with silicon carbide grinding paper, the samples were cleaned ultrasonically. Next, small 20 MHz lithium niobate transducers with gold wires soldered on them were bonded to the ends of each sample with a silica powder-filled epoxy, TRA-BOND 2151. This bonding agent was chosen because of its high viscosity and quick drying nature (it took about half a day to cure at room temperature) which allowed the formation of reliable bonds with little damage to the sample.

An aerogel sample is made through a catalyzed chemical reaction involving TMOS ($Si(OCH_3)_4$) and distilled water. To begin the process of making aerogel samples with 95% porosity, 0.73 ml of ammonia solution (containing 1 part ammonium hydroxide in 500 parts of distilled water) was first added to 7.3 ml of methanol. Then, 3 ml of TMOS (98%) was further added to the above solution to enable the following reaction to take place using ammonia as a catalyst:

$$Si(OCH_3)_4 + 2H_2O \rightarrow SiO_2 + 4CH_3OH \qquad (2.4)$$

When ultrasound is transmitted through aerogels with high porosity (>90%), large attenuation effects may be experienced [2.2]. Therefore, to achieve decent signals, the aerogels used in this work were grown in GCA samples. This was carried out by first lowering the GCA samples into the above solution with their pores perpendicular to the liquid surface. By allowing the solution to enter and fill the pores from one end through capillary action, the formation of bubbles within the pores could then be prevented. Each filled GCA sample was next placed in a short cylindrical stainless steel tube immersed in the same solution. The latter with the GCA sample inside was kept in a vial and left to gel in a covered beaker of methanol. This prevented the shrinkage of gel on the surface. After approximately 4 days, each GCA sample would be filled with and completely surrounded by a fair amount of wet gel confined in the stainless steel tube. Preparing the samples this way would prevent the ultrasonic signals that were sent through the aerogel-filled capillary pores from being affected by changes in the bulk neon lying outside. Each stainless steel tube together with all its contents may be considered as a single sample.

From eq. (2.4), it can be seen that the methanol produced in the reaction has to be removed from the wet gel. This was accomplished by keeping the gel in an autoclave system filled with methanol and heating the cell to 270 °C. Due to the rapid vaporization of methanol, the pressure builds up sharply to 2200 psi where it was prevented from further increase due to the presence of a relief valve. With the temperature held steady at 270 °C, the methanol vapor, whose critical temperature and pressure were 239.5 °C and 1173 psi respectively, was then released from the system very slowly (below 25 psi/min) under hypercritical conditions (see fig. 2.2) so that the delicate aerogel structure would not be damaged by surface tensions arising from the formation of liquid-vapor interfaces. Following this, the system was allowed to settle down to room conditions. Once ready, the aerogel was removed from the vial.

After the excess gel on the surface of the stainless steel tube was cleaned off with Q-tips, transducers were bonded onto the ends of the GCA sample without touching the metal tube. For a detailed description on the production of aerogels, please see ref. [2.2].

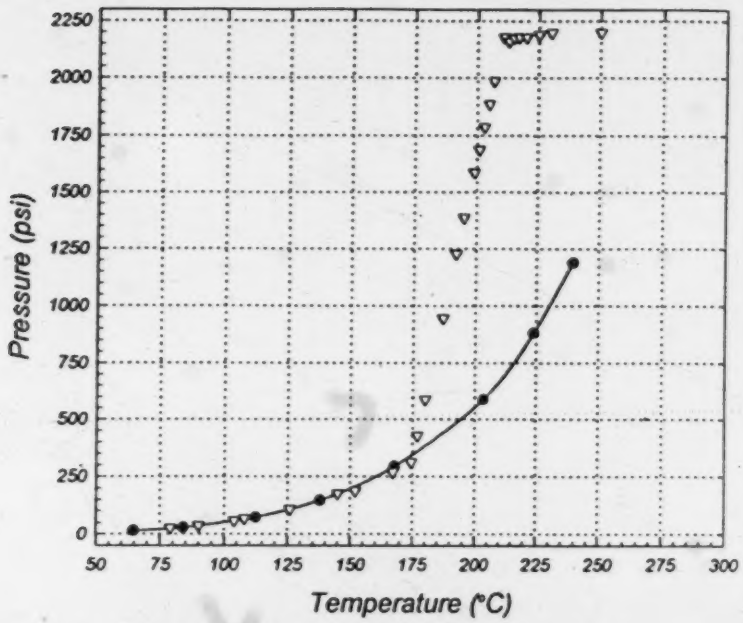

Fig. 2.2 Thermodynamic path taken during the production of aerogel.

Filled Circles = liquid-vapor coexistence curve of methanol and Inverted Triangles = actual path taken

2.3 Cryogenics and Thermometry

2.3.1 Refrigerator

Cooling was carried out by a CTI 8001 compressor and a CTI M-22 refrigerator, using helium gas as the working fluid. By delivering a stable cooling power, this system allows temperature control to within 0.01 K. In addition, the refrigerator has two stages so that very low temperatures can be achieved; in fact, the first and second stage can cool down to temperatures as low as 75 K and 10K respectively.

To simplify the explanation of how the refrigerator works, the latter will be represented by a piston, two valves and a regenerator. The regenerator is merely a heat exchanging matrix packed with a material of high surface area, high specific heat and low thermal conductivity. Its function is to extract heat from the incoming helium, store it and then return it to the outgoing helium.

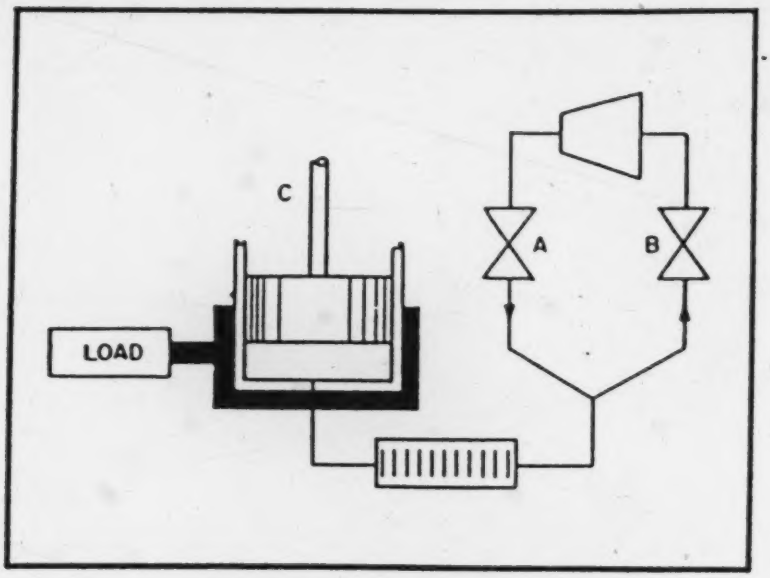

Fig. 2.3 Simplified diagram of the refrigerator

Compressed helium gas at room temperature is first supplied to the refrigerator by the compressor through valve A (see fig. 2.3) while the piston is at the bottom of its stroke. As the piston rises, the helium gas passes through the regenerator and fills the space beneath the piston. The matrix absorbs heat from the gas, thereby cooling it. At this point, the gas is approximately at the same temperature as the load. Valve A is then closed while valve B opens. The gas now expands into the low pressure discharge line and cools further. Heat then flows from the load through the cylinder walls into the gas. As the piston descends, the gas passes through the regenerator from which it receives more heat. The regenerator is subsequently cooled as the low-pressure gas returns to the compressor via valve B at approximately room temperature.

2.3.2 Experimental Cell

The experimental cell is made from oxygen free high conductivity copper, an excellent thermal conductor. It is mounted on top of a copper lid which is in turn connected to the second stage of the refrigerator through a brass thermal weak link. The purpose of the thermal weak link is to provide a long response time so that temperature fluctuation effects in each compressor stroke are minimized. Attached to the side of the lid is a 200 Ω heater. Since the refrigerator cooling power cannot be controlled, this heater is used to provide a variable heat supply to the cell so that its temperature can be held steady at any given setpoint. To shield the experimental cell from external blackbody radiation, a copper can enclosing the cell is fastened to the first stage. This shield is further contained within a vacuum can so that the cell can be thermally isolated from its surrounding. This is achieved initially by removing the air outside the cell until a pressure of about 70 mT is reached. During operation, the cold head itself acts as a cryopump to further prevent heat exchange with the exterior.

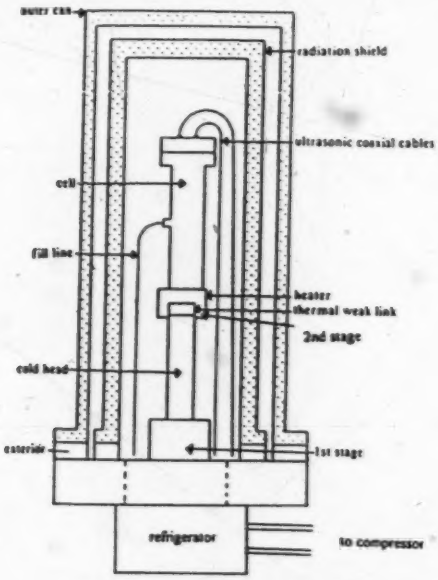

Fig. 2.4 The experimental cell

2.3.3 Thermometry

The thermometer used in this work is a calibrated platinum resistor (Lakeshore PT-103) glued inside a copper disk. The latter is then screwed onto a flat and smooth surface of the experimental cell with a thin layer of vacuum grease to ensure good thermal contact. Temperature measurements are processed by a digital resistance bridge (Quantum Design 1802). Through the use of the standard PID (Proportional, Integral, Differential) algorithm, this bridge which is connected to the heater mentioned above also serves as a temperature controller. In this work, the temperature needs to stay within 0.01 K of the desired setting for 60 s before data is taken.

2.4 Gas Delivery System

Neon gas of 99.996% purity enters the cell through a stainless steel tube soldered into a small brass fitting on the wall of the cell. A pressure transducer (Alpha 204) of 2 psi resolution is connected to the capillary system so that readings may be taken when required.

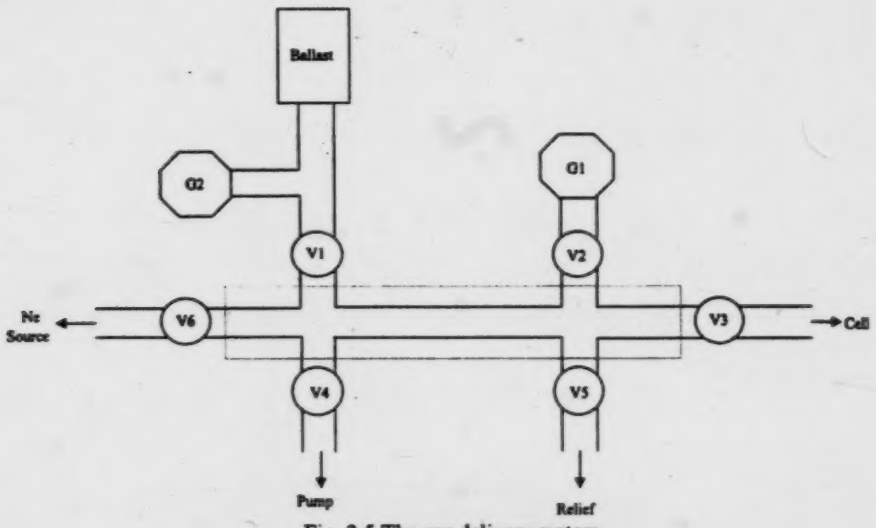

Fig. 2.5 The gas delivery system

Note: The pressure transducer mentioned above is denoted as G1

2.5 Determination of Gas Density

In order to map out the coexistence curve of neon, several constant density runs were made. This was accomplished by filling the cell with neon gas at 48 K (slightly higher than T_C) until a desirable pressure was attained. Ultrasonic measurements were then taken as the gas was cooled. The following procedure was used to determine the density of the neon gas after the filling for each run was completed.

To begin, a ballast of known volume (66.0 cm^3) was first used to calibrate the volume of the entire system (which comprises the cell, the capillary system and gauge G1), the cell itself, gauge G2 and part of the capillary system (shown within the dotted rectangle in Fig. 2.5). Initially, gauge G2 was not connected to the ballast and the whole setup was evacuated at room temperature. With valve V1 closed, about two atmospheres of neon gas was slowly admitted into the system. Once a steady pressure reading was achieved, valve V1 was opened until the next steady pressure reading could be taken. By using the ideal gas law, the volume of the entire system could then be determined. Similarly, the volume of the cell itself was also found. Following this, with pressure gauge G2 connected to the ballast, similar procedures were again followed to establish the volume of gauge G2 and part of the capillary system. The volume of the cell, gauge G2 and part of the capillary system were found to be 10.1±0.5, 2.4±0.1 and 2.6±0.1 cm^3 respectively.

Next, to obtain the total amount of gas in the cell with the latter maintained at 48 K, the entire system excluding the ballast was first filled with the required amount of neon gas. Valve V1 was next opened so that the ballast became filled with neon gas. Following this, valves V2 and V3 were shut. After equilibrium was reached, the ballast pressure and room temperature readings were taken so that the amount of gas within gauge G2, the ballast and part of the capillary system could be determined from the Virial equation

$$PV = nRT\left(1 + n\frac{B}{V}\right) \qquad (2.5)$$

B, the first Virial coefficient for neon, was determined by A. Michels *et al.* [2.4] as 11.4 cm^3mol^{-1} at 298.16 K; incidentally, this value is valid for pressure readings up to 2900 atm. Valve V4 was next opened so that the ballast could be evacuated and the above procedure repeated until the cell was almost empty. Eventually, by plotting the pressure of the system against the total amount of neon removed after each step, the initial amount and thus the density of gas within the cell could be found by extrapolating the linear portion of the graph where the pressure readings were low. The inset in fig. 2.6 shows the nearly ideal gas behavior of neon at 48 K and very low pressure.

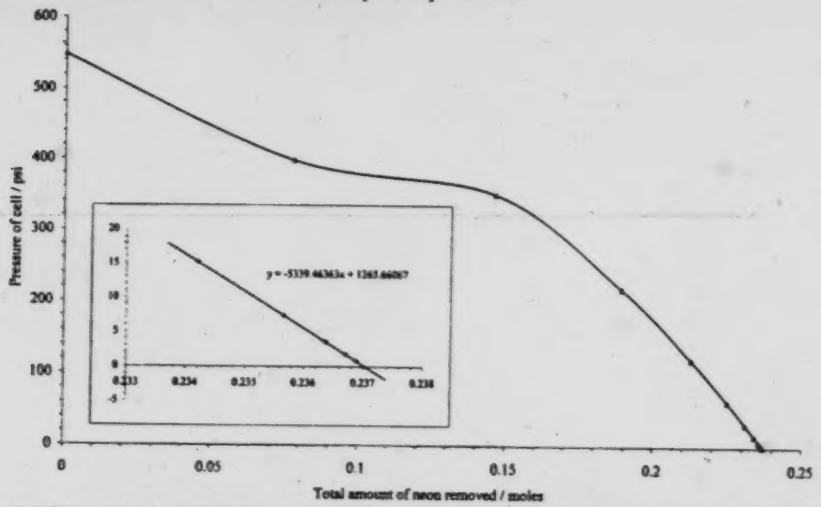

Fig. 2.6 Determination of total amount of gas in the system. Here, the system was initially filled at 48 K until a pressure of 548.0 psi was achieved. The inset magnifies the linear portion of the curve.

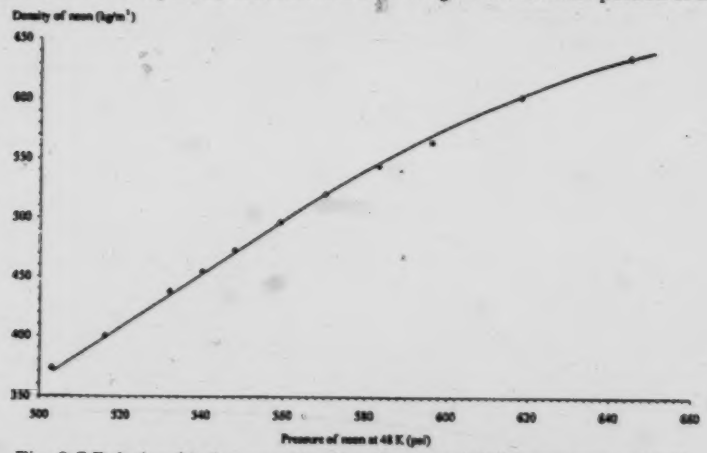

Fig. 2.7 Relationship between density of neon and filling pressure at 48 K

2.6 Ultrasonics

In this work, only changes in sound velocity and attenuation are considered. Their absolute values are not used as these cannot be determined to a satisfactory degree of accuracy. For example, it is not possible to obtain absolute sound speeds precisely using the transit times of the sound waves through the sample. This is because the transducer bonds at the ends of the sample possess finite thicknesses and thus make non-negligible contributions to the transit times and attenuation of the signals.

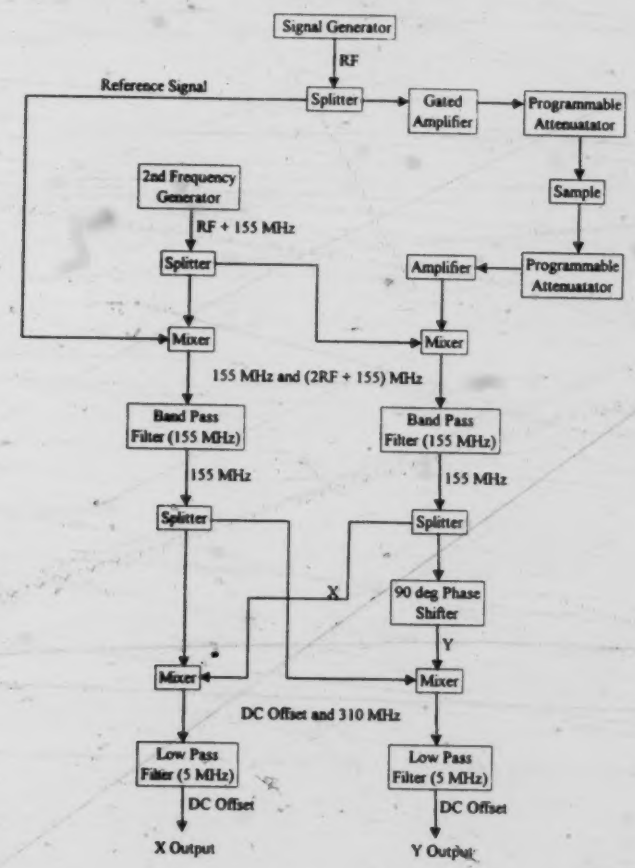

Fig. 2.8 Schematic of the ultrasonic system

To see how relative sound speeds can be determined precisely, suppose the velocity of an ultrasonic signal in a sample is given as $v_o=L/t_o$ where L is the length of the sample and t_o the transit time. Then for any velocity v, we have $v/v_o=t_o/(t_o+\Delta t)$ where Δt is the change in transit time. Since $\Delta t=\Delta\phi/\omega$ where $\Delta\phi$ is the phase change and ω the angular frequency of the sound wave, we can now express the relative speed of the ultrasonic signal in terms of its phase change:

$$\frac{v}{v_o} = \frac{1}{1+\Delta\phi/\omega t_o} \qquad (2.6)$$

Using a phase-sensitive pulse-echo technique, small changes in the ultrasonic attenuation (0.01 dB resolution) and velocity (few parts in 10^6) can then be determined.

The frequency generator produces a continuous radio frequency (RF) wave which is split into a sample signal and a reference signal. The sample signal is converted into a series of pulses by the gated amplifier. These pulses have a specified duration of about 2.5 μs and are produced at a repetition rate of 500 per second. To prevent sample heating, the amplitude of the pulses need to be adjusted to appropriate levels by a number of programmable attenuators before the signals reach the sample.

These pulses are sent to the cell via coaxial cables connected to electrodes on the sample holder. Inside the cell, the signals propagate to and from transducers attached to the samples through thin gold wires. The piezoelectric transducer at one end of the sample turns the electrical pulses into sound waves which are then transmitted through the sample to the receiving transducer. After undergoing a series of amplification and attenuation, the received signal is then ready to be used.

To measure sound velocity, the received signal must be separated into components in-phase (x) and 90^0 out of phase (y) with respect to the reference signal. Unfortunately, phase shifters generally operate only within a narrow band of frequencies so that a heterodyne system needs to be employed. In such a system, a second frequency generator is used to produce a continuous wave at frequency RF+155 MHz. This wave is split into two: one mixed with the received signal and the other with the reference signal. Both signals now comprise 155 MHz and 2RF+155 MHZ components. By passing these waves through filters centered at 155 MHz, all the signals are eventually converted to 155 MHz regardless of their initial RF values. This way, only one 155 MHz phase shifter is needed for all the velocity measurements.

After the 155 MHz received signal is divided into its x and y components, the individual components are mixed with the reference signal so that two resultants are produced from each mixing: a useful DC offset and a 310 MHz signal that is filtered out. The attenuation α and phase ϕ of the received signal are finally given as follows:

$$\alpha = 10\log(v_x^2 + v_y^2) \qquad (2.7)$$

$$\phi = \tan^{-1}(\frac{V_y}{Vx}) \qquad (2.8)$$

where V_x and V_y are the DC voltages of the x and y components respectively.

In each run, all the desired frequencies were scanned before moving to the next temperature. While equilibrating to the next temperature, similar data were taken on a fixed attenuator. This drift data which would eventually be subtracted from the sample data was needed to eliminate long term shifts in electronic measurements due to room temperature fluctuations. In addition, short term drift was eliminated by establishing an active baseline before and while taking data. For each data point, signal averaging was done over at least 2000 pulses.

2.7 Determination of Surface Area

To ensure that the pores in the GCA samples were completely filled with aerogel, a simple test was devised to determine the surface area per unit weight of the aerogel. If the value obtained was too small, say less than 100 m^2/g, we would know that the aerogel did not completely fill the pores.

Consider a porous solid with mass M and density ρ_p. If n moles of gas with molecular mass m are adsorbed onto the sample, the system's effective density becomes:

$$\rho_e = \rho_p[1 + \frac{nm}{M}] \qquad (2.9)$$

This expression holds as long as the thickness of the adsorbed film is much less than the viscous penetration depth (see eq. (1.34)) of the gas so that the adsorbate and the substrate are always viscously locked together. Because for ultrasonic sound waves at 7.7 MHz, the penetration depth of liquid neon at 27 K ($\eta \approx 125$ μPa-s and $\rho_f \approx 1205$ kg/m^3) may be worked out using eq. (1.34) as approximately 65 nm, this condition is certainly satisfied even for films of several monolayers thick.

Since Biot's [1.10] theory of sound propagation shows that the modulus effect of a fluid film is negligible provided that the pressure of the gas remains small compared to its saturated value, we may write the longitudinal sound speed of the system as:

$$v_l^2 = \frac{K_p + 4/3\mu_p}{\rho_e} \qquad (2.10)$$

Upon substituting eq. (2.9) into (2.10), we obtain:

$$\frac{n}{M} = \frac{1}{m}[(\frac{v_{lo}}{v_l})^2 - 1] \qquad (2.11)$$

where v_{lo} is the sound speed in the medium before any gas is introduced.

A complete adsorption isotherm can be constructed by plotting v_l/v_{lo} versus P/P_o. If the BET model [2.5], which is based on a kinetic picture of the adsorption process, is used, we may then analyze the linear portion of the adsorption isotherm with the equation

$$\frac{P/P_o}{(n/m)(1-P/P_o)} = \frac{1}{(n_m/M)c} + \frac{(c-1)}{(n_m/M)c}\frac{P}{P_o} \qquad (2.12)$$

Here, n_m is the number of moles of adsorbate required to make up one monolayer and c is a dimensionless parameter characterizing the strength of interaction between the adsorbate and the substrate. Clearly, the monolayer capacity n_m/M and the parameter c may be made known by plotting the term on the left hand side of eq. (2.12) against P/P_o. With this information, the specific surface area of the sample may be calculated using

$$\frac{S}{M} = \frac{n_m}{M} N_a \sigma \qquad (2.13)$$

where N_a is the Avogadro's number (6.023×10^{23} mol^{-1}) and σ the areal coverage of the adsorbate molecule (taken as 8 A^2 for neon).

Chapter 3: Results and Analysis

3.1 Surface Area Determination

Fig. 3.1 and 3.2 show the adsorption isotherm and BET plots obtained for an aerogel-filled GCA sample using 7.68 MHz longitudinal waves.

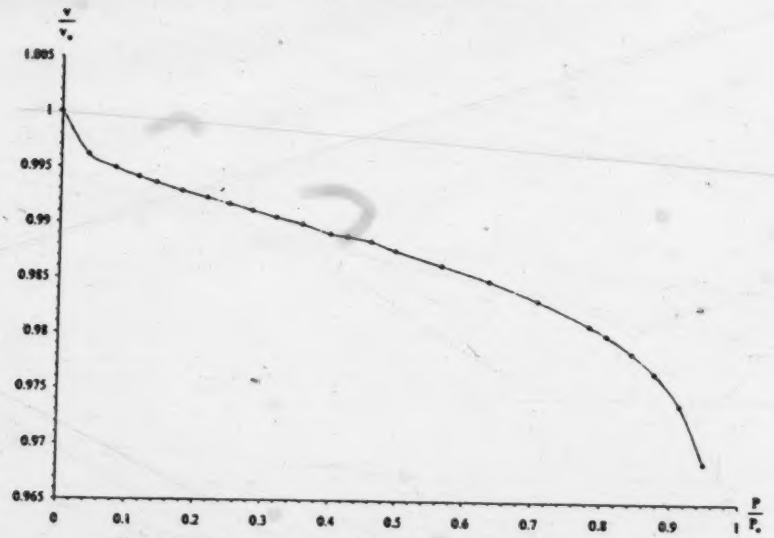

Fig. 3.1 Adsorption isotherm of neon at 27 K (s.v.p. is 14.28 psi)

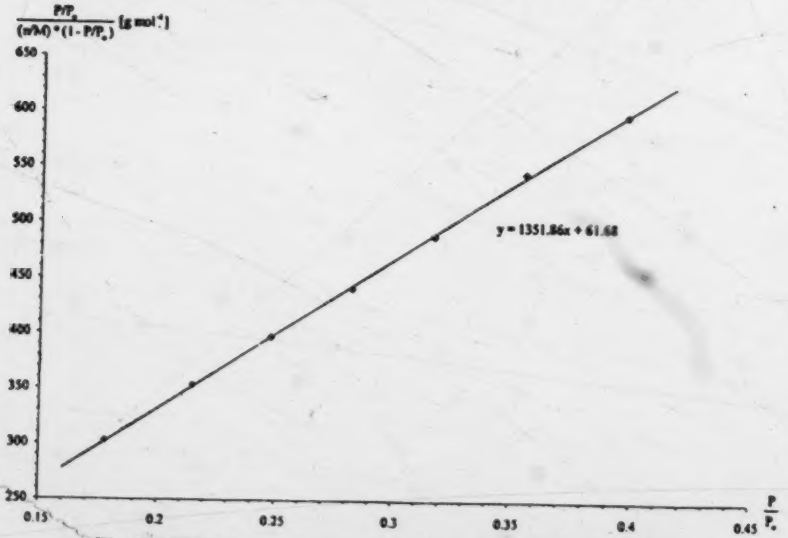

Fig. 3.2 BET plot for neon confined in aerogel-filled GCA sample

Using eq. (2.12), the monolayer capacity and dimensionless parameter were found to be 707×10^{-6} mol/g and 22.9 respectively. The surface area per unit mass of the whole sample was calculated using eq. (2.13) as 34.1 m^2g^{-1}. If the volume of the whole sample and the density of the aerogel were denoted as V and ρ_A respectively, then the mass of the aerogel trapped within the sample would be given as $\rho_A \phi V$ whilst the mass of the GCA sample alone would be $\rho_p V$. Also, we could approximate the total mass of the sample with the mass of the GCA glass alone. With the above information, the surface area per unit mass of aerogel might be expressed as

$$\frac{S}{M_{aerogel}} = \frac{\rho_p}{\phi \rho_A} \frac{S}{M_{total}} \qquad (3.1)$$

Using the values quoted in sec. 2.1, the above quantity was found to have a value of 755 m^2g^{-1}. This value seemed reasonable (see sec. 1.2) and probably indicated that the GCA sample was completely filled with aerogel.

3.2 Properties of Near-Critical Neon

To analyze and interpret the experimental results obtained in this work, some relevant properties of near-critical bulk neon must first be known. The correlation length amplitude (ξ_o) and the critical exponent (ν) of Ne are about 0.25 nm and 0.63 respectively [3.1]. With the current experimental setup, temperature control of up to 0.01 K of each setpoint is easily achievable. Thus, using eq. (1.18), a temperature measurement that is 0.01 K away from the critical value will yield an approximate value of 50 nm for the correlation length of neon. Such a length scale is certainly much smaller than the pore size of the GCA samples but comparable in magnitude to typical pore sizes of aerogels. In other words, although the behavior of neon is bulk-like when it is confined in GCA samples, it will certainly be altered when it is confined in aerogels.

Another property we may want to consider is the viscous penetration depth of near-critical neon. Since the critical viscosity and density of neon are about 25 μPa-s [3.2] and 484 kg/m^3 [3.3] respectively, its viscous penetration depth for sound waves at 5 MHz frequency may then be calculated using eq. (1.34) as 57 nm. This value is again much smaller than the pore size of the GCA samples but comparable in magnitude to typical pore sizes of aerogels. In this high frequency regime (see sec. 1.6), near-critical neon is not expected to couple viscously to the pore surfaces of either sample. However, inertial coupling is still present in both the SH and L modes.

3.3 Ultrasound in Bulk Neon Confined in GCA Channels

Fig. 3.3 and 3.4 show what was observed when ultrasound in the SH mode was transmitted through a GCA sample whose pores contained neon vapor at varying temperatures. The curves have been displaced vertically for clarity. Three different densities corresponding to values below, close to and above the critical density of neon are shown here. Unfortunately, a study on the frequency-dependence behavior of the different sound modes could not be carried out as decent signals could only be obtained for a very narrow range of frequencies.

It was observed that hysteretic effects in the velocity changes were most pronounced when the neon vapor density was below the critical value. At the critical density itself, the diminution of hysteresis was clearly related to the disappearance of surface tension, as pointed out in sec. 1.4. No simple explanation however could be found for the disappearance of hysteresis when the density was above the critical value.

As the neon vapor was cooled, sharp cusps signaling phase transitions were seen in the velocity changes. Furthermore, when the neon vapor density got closer to the critical value, the magnitude of the change in velocity also increased correspondingly. The warming phase, on the other hand, did not reveal any sharp turning points.

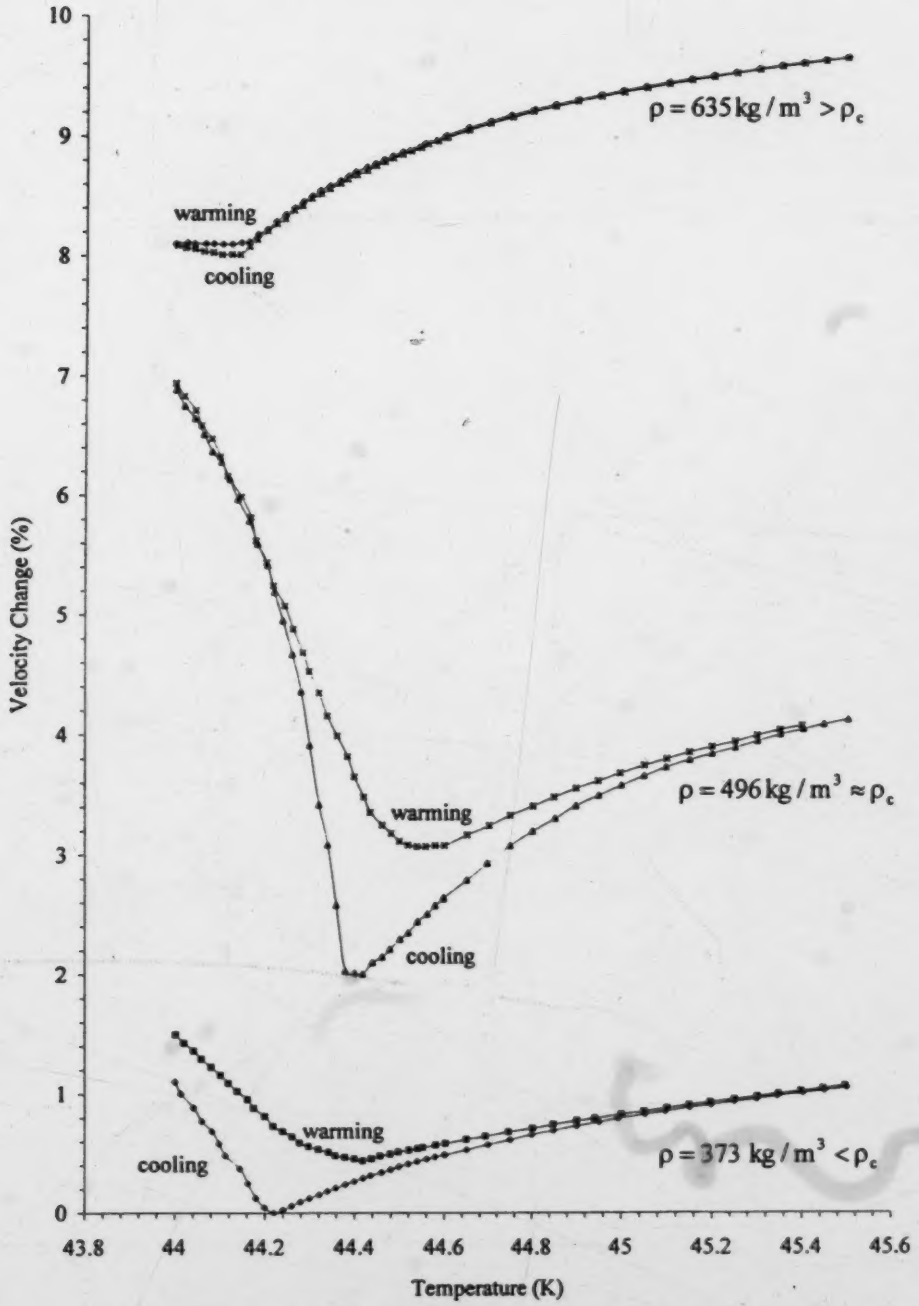

Fig 3.3 Sound velocity change observed when sound waves (3.4 MHz) in the SH mode were propagated in bulk neon. Curves are displaced vertically for clarity.

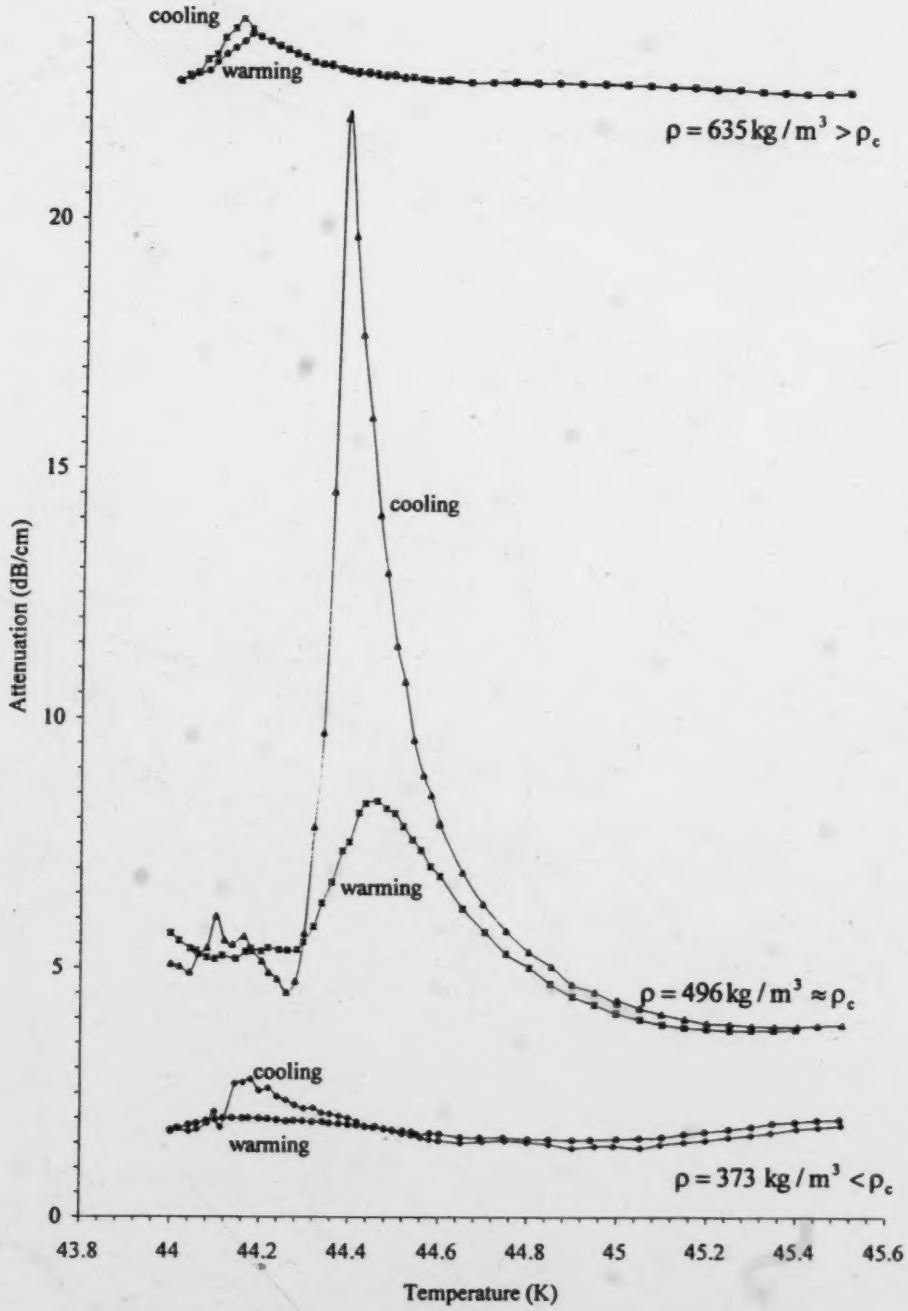

Fig 3.4 Attenuation observed when sound waves (3.4 MHz) in the SH mode were propagated in bulk neon. Curves are displaced vertically for clarity.

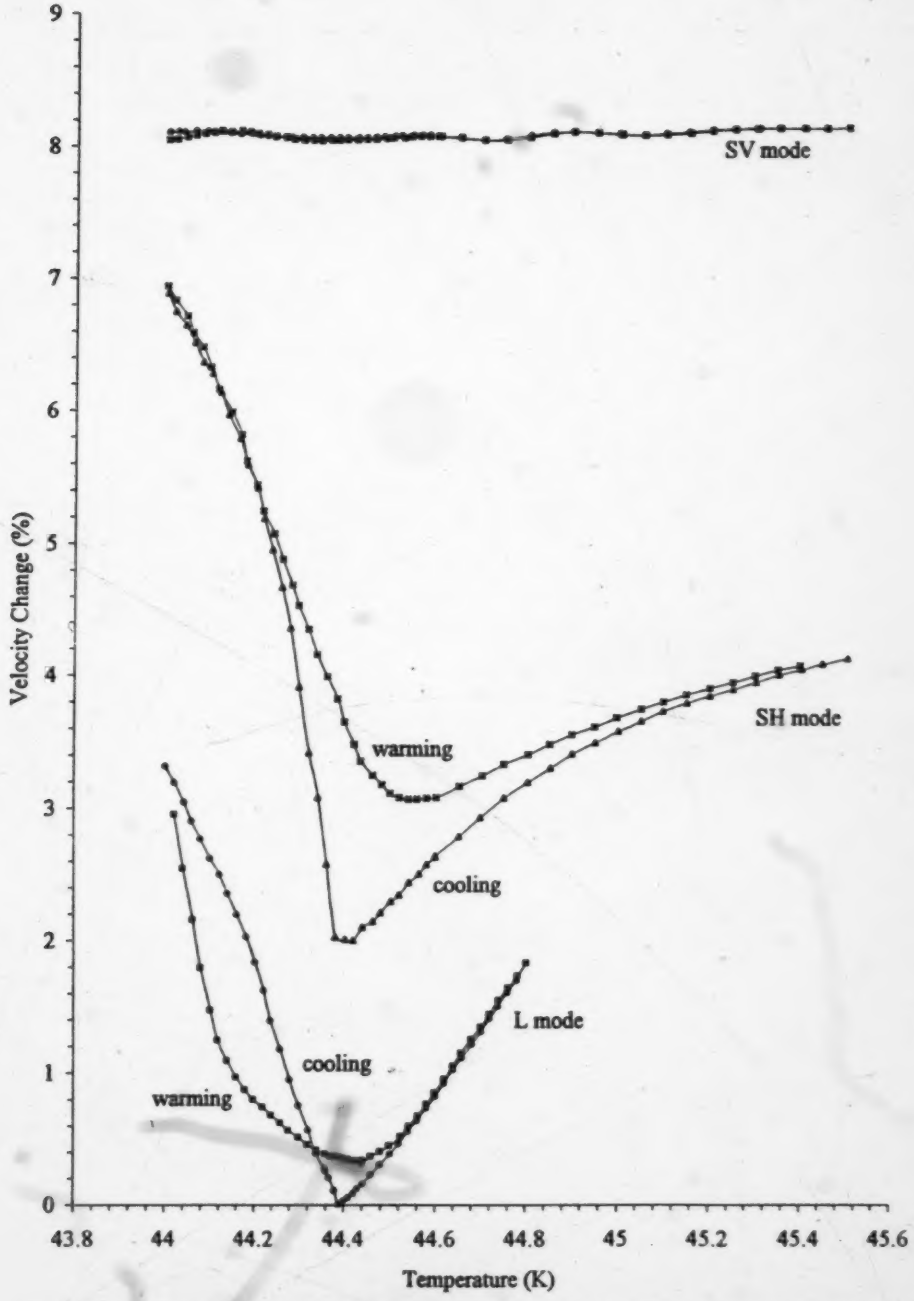

Fig 3.5 Sound velocity change observed when sound waves in the SH (3.4 MHz), L (12 MHz) and SV (9.2 MHz) modes were propagated in bulk neon of density 496 kg/m^3

Curves are displaced vertically for clarity.

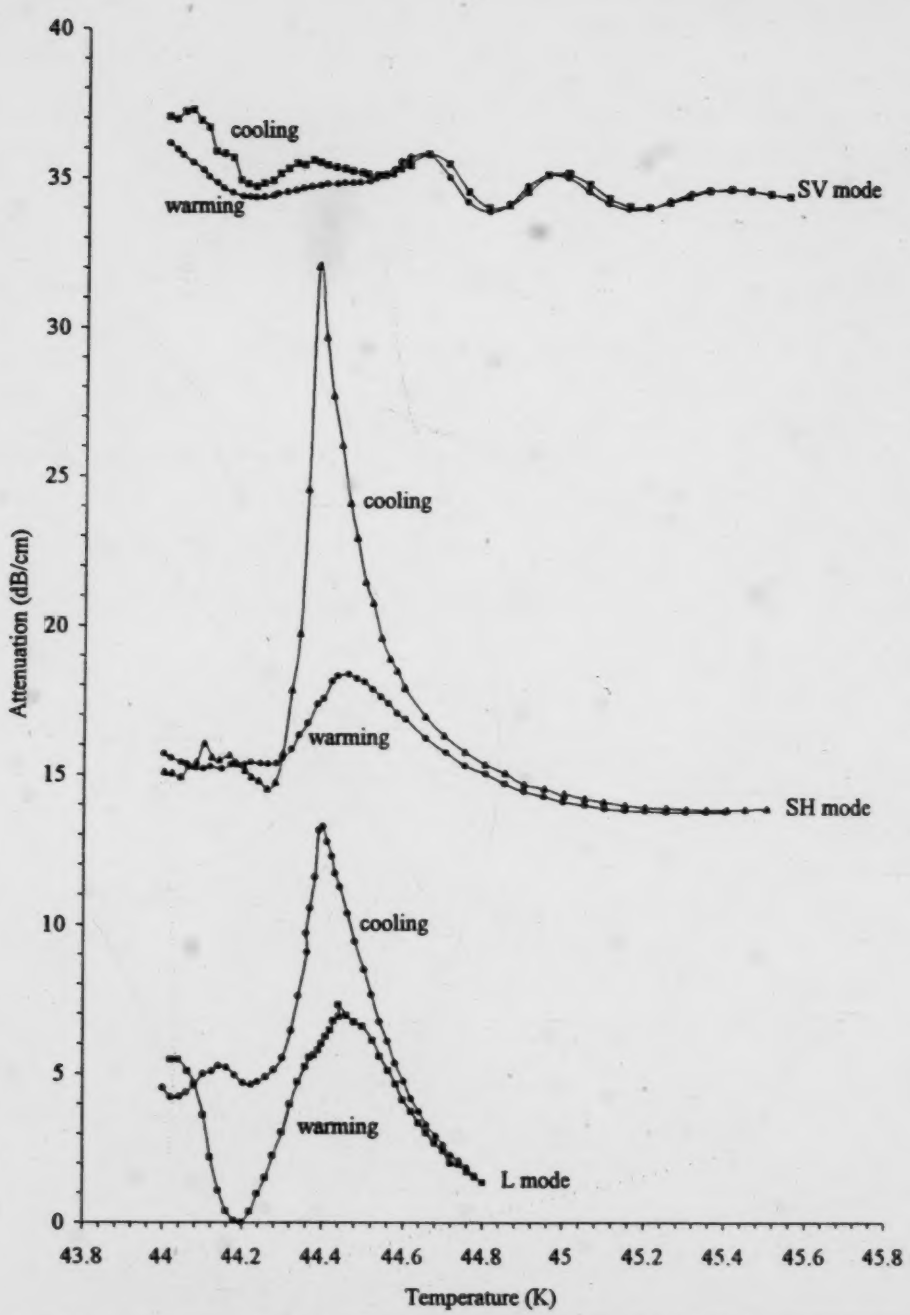

Fig 3.6 Attenuation observed when sound waves in the SH (3.4 MHz), L (12 MHz) and SV (9.2 MHz) modes were propagated in bulk neon of density 496 kg/m^3.

Curves are displaced vertically for clarity.

Sharp peaks were obtained for the attenuation curves during the cooling phase only when the neon vapor density was near or greater than its critical value. Like the velocity curves, the strongest attenuation (about 18 dB) was registered near the critical point. Ultrasonic attenuation during the warming phase was generally much smaller than what was observed in the cooling phase unless the neon vapor density was higher than its critical value.

The L mode demonstrated almost the same behavior as the SH mode, and since no new information could be gleaned from it, only data obtained near the critical point are shown in fig. 3.5 and 3.6. For the SV mode, no significant features were seen in either the velocity or attenuation curves even when the neon vapor density was very close to its critical value.

If near-critical fluids were so compressible, we would not expect them to move rigidly with the pores. An apparent decrease in the density of the medium leading to the formation of velocity peaks should thus have occured. But that was not what we saw! Furthermore, the relatively huge magnitudes of velocity change could not be easily accounted for. In sec. 1.4, it was pointed out that sound velocities are affected only by changes in the effective density and elastic modulus of the medium. Since the shear and bulk moduli of liquid neon (~ 10^6 Pa) are both much smaller than that of glass (~ 10^{10} Pa), we can almost rule out modulus effects. This leaves us with the only other possibility: a sharp peak in the medium density at each transition point must have contributed to a corresponding strong dip in the velocity change. Using eq. (1.30), a 2.5% change in sound speeds ($\Delta v/v$) will correspond to a 5% change in the effective density of the medium ($\Delta\rho/\rho_{total}$). After inserting suitable values quoted in sec. 2.1 into eq. (1.32), we arrive at the conclusion that an approximately 16% change in the density of neon ($\Delta\rho/\rho_{neon}$) is required to explain the observed phenomenon here. Nevertheless, it is not easy to account for the density effects. The following are some possible but incorrect explanations on how these effects could have occured. It may be argued, for example:

- *That movement of neon fluid between the capillary system and the cell could have caused the formation of peaks in neon density as the temperature was lowered.*

  However, it must be pointed out that the volume of the cell (~ 10.1 cm^3) was fairly large compared to that of the capillary system (~ 2.6 cm^3). Besides, the huge difference in the temperature of the capillary system (~ 298 K) and the cell (~ 44 K) meant that a massive exchange of neon fluids would be needed to justify the 16% change in neon density within the cell.

- *That capillary condensation occured in the GCA pores.*

  But this process could not have occured above the critical temperature where large velocity drops were also observed. Furthermore, there was no reason for the velocity to increase again below each transition temperature.

- *That a thick adsorbed film of neon was built up in the GCA pores initially due to van der Waals forces.*

  However, the diameter of the pores was 10 μm so wetting films of order 1 μm thick would be needed to account for the density effects. And van der Waals forces could simply not hold up films this thick.

- *That the presence of liquid neon droplets on the transducers or the formation of a moving meniscus in the bulk neon outside the sample could lead to spurious effects on the velocity and attenuation measurements.*

  Then again, substantial changes in the ultrasonic signals were observed above the critical temperature where there could not be any liquid phase in the bulk neon outside the sample. Also, these changes were simply too large and systematic for this argument to be plausible.

- *That the neon fluid might not be coupled to the pore surfaces initially. But as the temperature was lowered, it could become coupled to the pore walls and then be decoupled again after the phase transition.*

Such an explanation could not be true since inertial coupling was definitely present (recall tortuosity $\tau \to \infty$) in both the SH and L modes.

- *That steep density gradients within the cell could be formed in the presence of gravity since near-critical fluids are highly compressible. Consequently, changes by as much as 16% in the neon density over the sample height (~ 1 cm) due to the lowering temperature could lead to the observed phenomenon.*

To estimate how close to the critical temperature we need to be for substantial density gradients to develop over the sample height, the following relation [3.4] may be used

$$t = (\Gamma \rho_c g h / B P_c)^{1/(\beta+\gamma)} \qquad (3.2)$$

Here, B is the amplitude fit in eq. (1.19) whilst Γ and γ appear in the relation between the fluid's isothermal compressibility κ_T and the reduced temperature $t>0$:

$$\kappa_T = \Gamma t^{-\gamma} \qquad (3.3)$$

Using values quoted in ref. [3.5], we found t to be 1.2×10^{-4}. In other words, at the critical density of neon, we needed to get as close as 0.005 K to the critical temperature in order to observe such gravitational density effects. Since steep velocity changes began to take place in the sample at temperatures as far as 0.4 K away from the critical temperature for neon densities close to the critical value, this argument would not hold water.

Having exhausted almost all the different possibilities, we must now turn to the compressibility peak of near-critical neon for a plausible explanation. If the ultrasonic velocity in near-critical neon is about 100 m/s [1.17], then at 4 MHz, the wavelength of the sound waves will be about 25 μm. This value is comparable in magnitude to the pore size of the GCA samples and may be even smaller as we get closer to the critical temperature (see fig. 1.3). Near-critical neon may therefore not move rigidly with the GCA pores since it is very compressible.

However, how this sloshing of a highly compressible, near-critical fluid is related to the sharp velocity dips or attenuation peaks of the ultrasonic signals is still beyond our comprehension. We are only certain that the phenomenon is somehow related to an increase in the adiabatic compressibility (see sec. 1.3) of the near-critical fluid, the high frequency (in the order of MHz) of sound employed and the large size (~ 10μm) of the GCA pores. Although it was not our intention to measure the adiabatic compressibility of near-critical neon, we were indirectly doing that when we took those ultrasonic measurements. Hence, the velocity dips and attenuation peaks observed could still serve as effective markers for the coexistence curve of neon.

The fact that the L mode demonstrated almost the same behavior as the SH mode was hardly a surprise since the polarizations of both modes were perpendicular to the pore walls. The same sort of sloshing motion in the neon fluids was therefore expected to take place.

The absence of any significant features in the sound velocity and attenuation plots for the SV mode were due primarily to two factors: firstly, the polarization of this mode was parallel to the pore axis so that sloshing could not be very significant, and secondly, near-critical neon was not expected to couple viscously to the pore walls (see sec. 3.2). In fact, if we could gauge the upper limit of the viscous attenuation on the sound signal, we would not expect any huge viscous effects to be present in the first place. Since we were in the high frequency regime, relevant values quoted in sec. (2.1) and (3.2) might be substituted into eq. (1.36) to carry out this estimation. At a sound frequency of 9.2 MHz, the maximum possible amount of viscous attenuation was worked out as 2 dB/cm. The experimental results obtained clearly support such an estimate. To go one step further, the lack of viscous effects in the SV mode also argued that such effects could not be responsible for the behavior of the sound signals in the other two modes. This also meant that the sharp attenuation peaks observed in the other modes could only be due to the dissipation of radiated sound energy in the sloshing fluids.

3.4 Ultrasound in Neon Confined in Aerogels in GCA Channels

Fig. 3.7 to 3.10 show the results for both the SH and L modes in neon when it was confined within aerogel of 95% porosity. No decent signals could be detected for the SV mode in near-critical neon. Again, three density values (below, near and above the critical point) were chosen for each mode to reflect the general behavior of ultrasonic signals within each regime. Unfortunately, distinct signals could again be obtained only for a very limited range of frequency. It is also interesting to notice that the SH and L modes here have much less in common than that in bulk neon. Up to this point, very little understanding has been established on the behavior of the different sound modes in neon-filled aerogel.

Hysteresis was seen in the velocity curves of the SH mode when the density of neon was below its critical value within the aerogel; this phenomenon however gradually disappeared as we got closer to the critical point. On the other hand, hysteresis in the L mode did not vanish until some density value higher than the critical one was attained. Strangely enough, distinct troughs, similar to those observed in bulk neon, surfaced only in that regime for the L mode. Apart from that, no sharp peaks or troughs were observed in the velocity curves of both modes; the strange shapes of these curves proved to be totally unexpected.

Only the attenuation curves showed those familiar distinct peaks corresponding to neon fluid phase transitions within the aerogel. Below the critical point, warming curves for both modes did not reveal any sharp peaks and above the critical point, the attenuation magnitudes began to decrease rapidly.

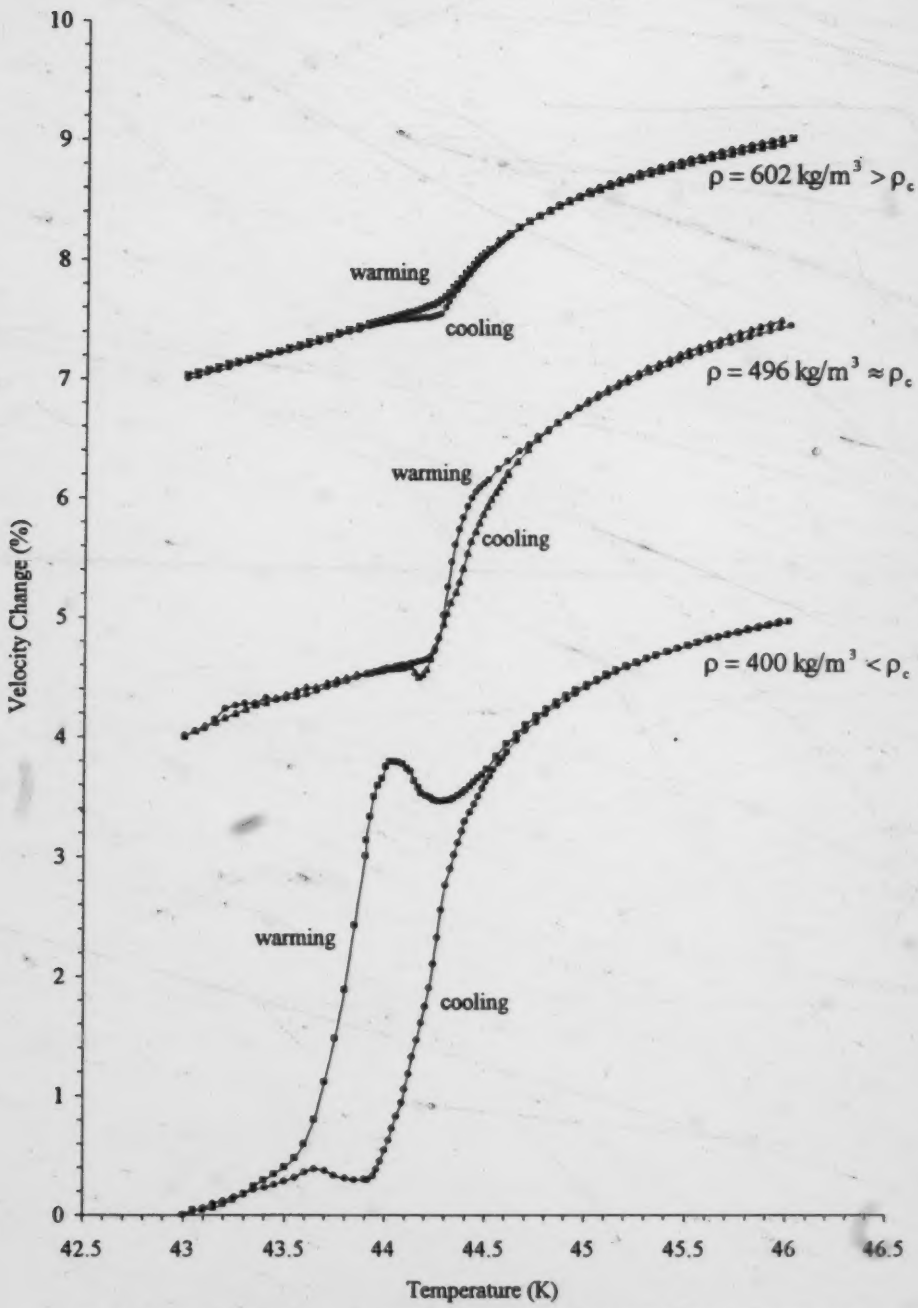

Fig 3.7 Sound velocity change observed when sound waves (3.7 MHz) in the SH mode were propagated in neon confined within 95% aerogel

Curves are displaced vertically for clarity.

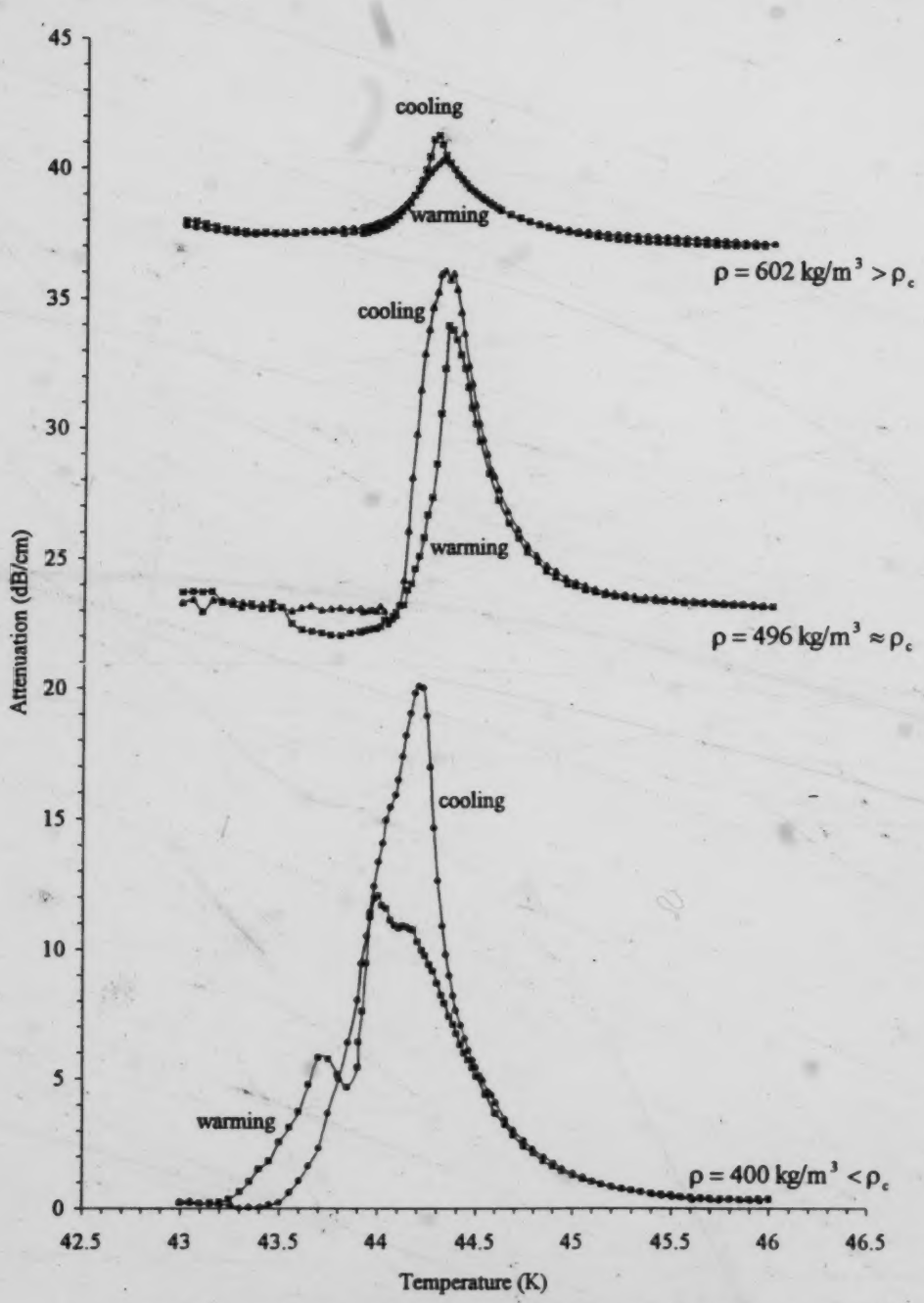

Fig 3.8 Attenuation observed when sound waves (3.7 MHz) in the SH mode were propagated in neon confined within 95% aerogel

Curves are displaced vertically for clarity.

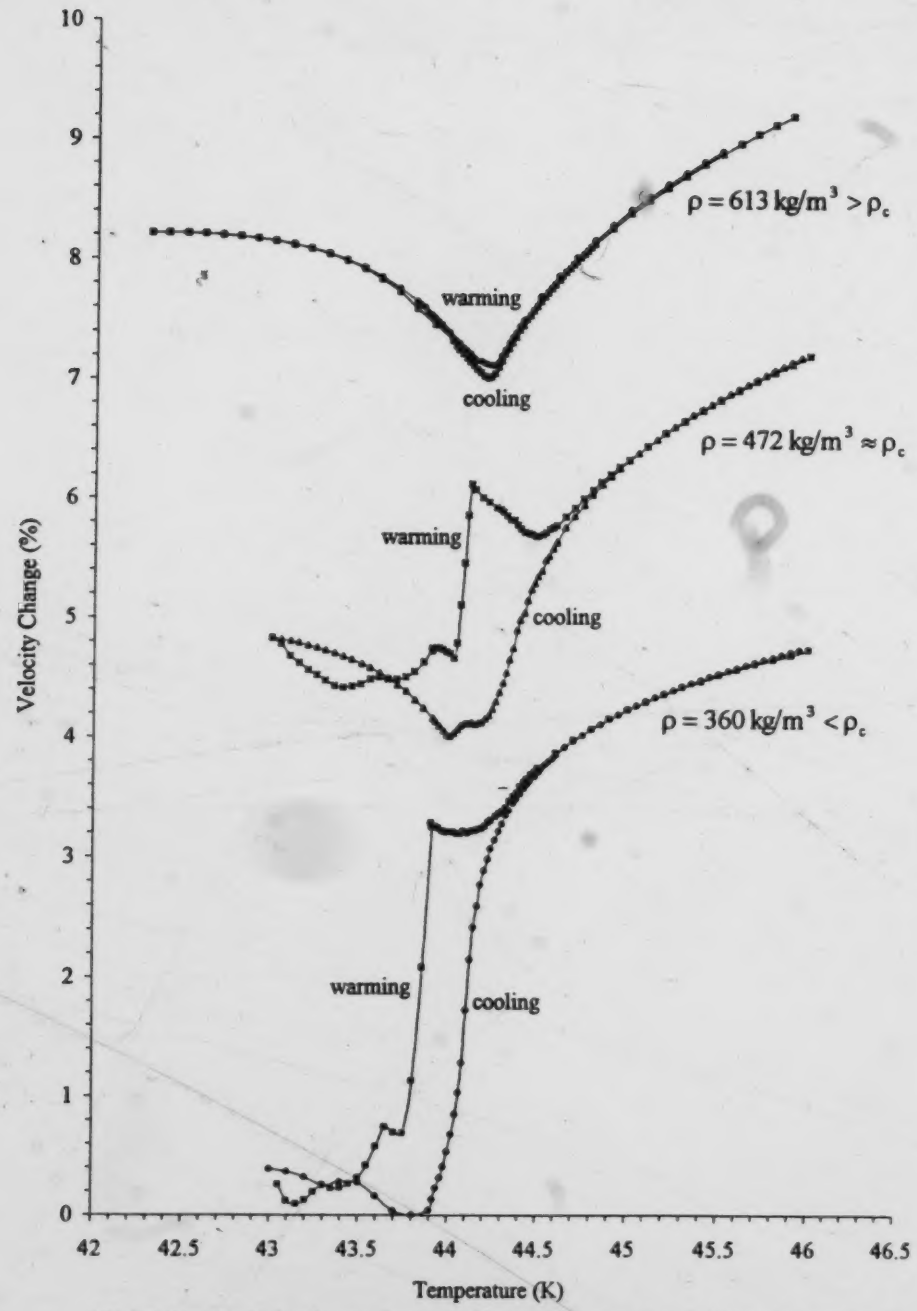

Fig 3.9 Sound velocity change observed when sound waves (5.5 MHz) in the L mode were propagated in neon confined within 95% aerogel

Curves are displaced vertically for clarity.

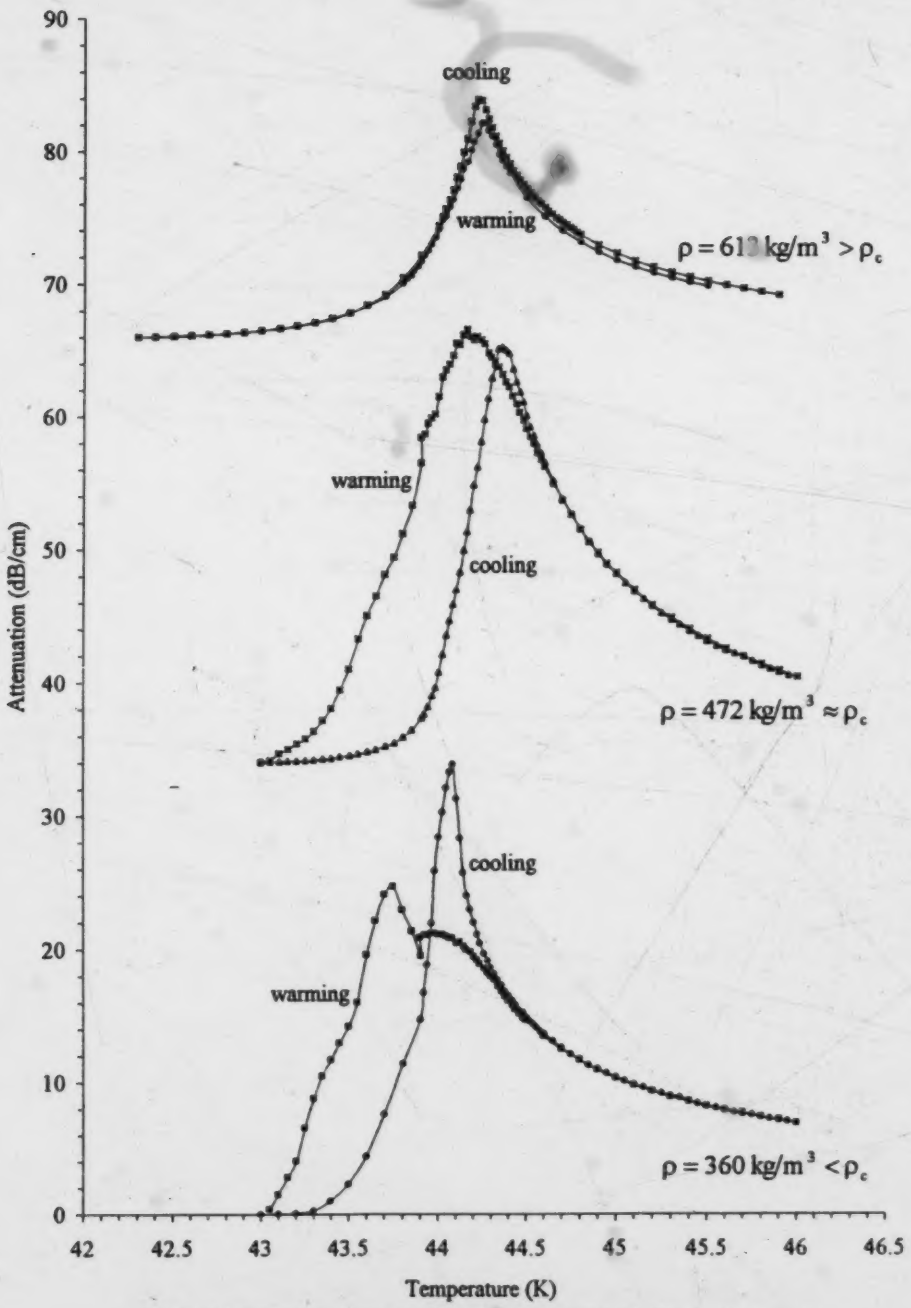

Fig 3.10 Attenuation observed when sound waves (5.5 MHz) in the L mode were propagated in neon confined within 95% aerogel

Curves are displaced vertically for clarity.

Sloshing of the highly compressible neon fluid could still occur (maybe to a smaller extent) in the aerogels since the fluid was not viscously coupled to the pore surfaces (see sec. 3.2). In fact, it was even quite conceivable for the aerogel structure to move with the sloshing neon since the former was fairly compliant. Based on figures quoted in sec. (2.1) and (3.3), the elastic modulus $K=\rho v^2$ of aerogels with 95% porosity was determined to be an order of magnitude smaller (~ 4×10^5 Pa) than that of near-critical neon (~ 5×10^6 Pa).

3.5 Coexistence Curves of Bulk and Confined Neon

To define the coexistence curve for bulk neon, several detailed density runs were made for the SH mode. Likewise, for confined neon, many density runs were carried out in the L mode. Since both sound modes behaved the same way, it did not really matter which mode was ultimately chosen for this purpose. In all the runs, peaks in the attenuation curves during the cooling phase were used as indicators of phase change. If sharp minima were seen in the velocity curve, the data would be used to confirm the results from the attenuation curves; but this was seldom the case for confined aerogel (see sec. 3.4). The turning points in the warming curves unfortunately were not nearly as sharp as those in the cooling ones, so the coexistence curves derived here would apply only for the condensation processes.

An attempt to fit the bulk curve with eq. (1.19) yielded B=0.413, ρ_c=490 kg/m^3, T_c=44.40 K and β=0.415. On the other hand, the figures obtained by Chan *et al.* [3.5] were B=1.425, ρ_c=484 kg/m^3, T_c=44.48 K and β=0.327. The huge discrepancies between the exponents and amplitude fits could be attributed to the asymmetry of the actual bulk curve which tends to be broader on the right edge than the left (see Fig. 3.12). Since this model assumed symmetry properties, it would not seem so appropriate for the results here unless very dense data closed to the critical point were used. In fact, it was never our intention in the first place to make a precision study of near-critical bulk neon. The recorded differences merely served as an indication of the limited accuracies of our temperature (± 0.01 K) and density (± 20 kg/m^3) measurements.

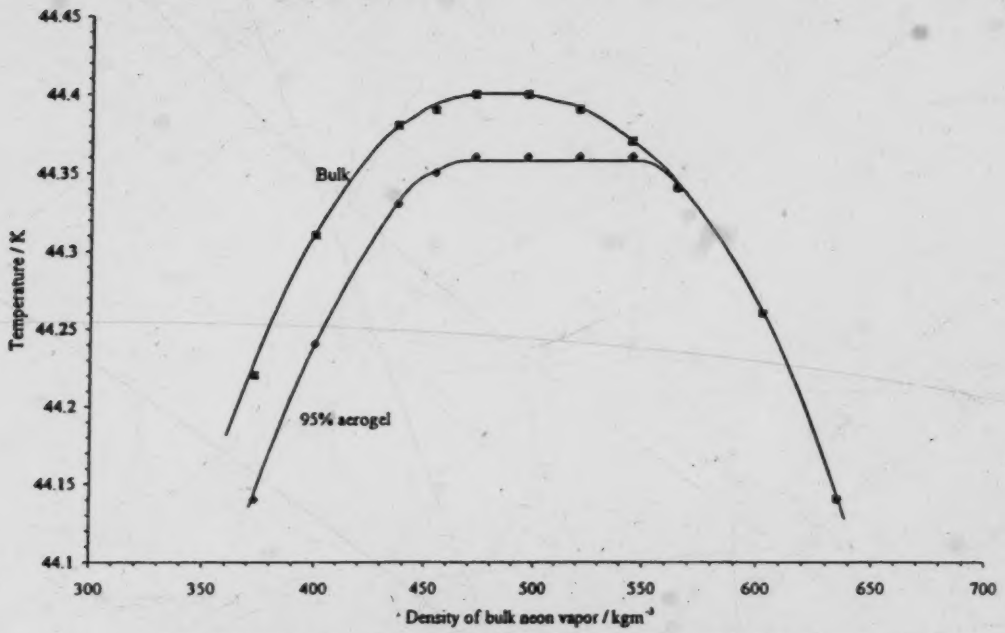

Fig 3.11 Coexistence Curves of Bulk Neon and Neon Confined in 95% Aerogel.

The last 3 data points on the high density edge actually belong to both curves.

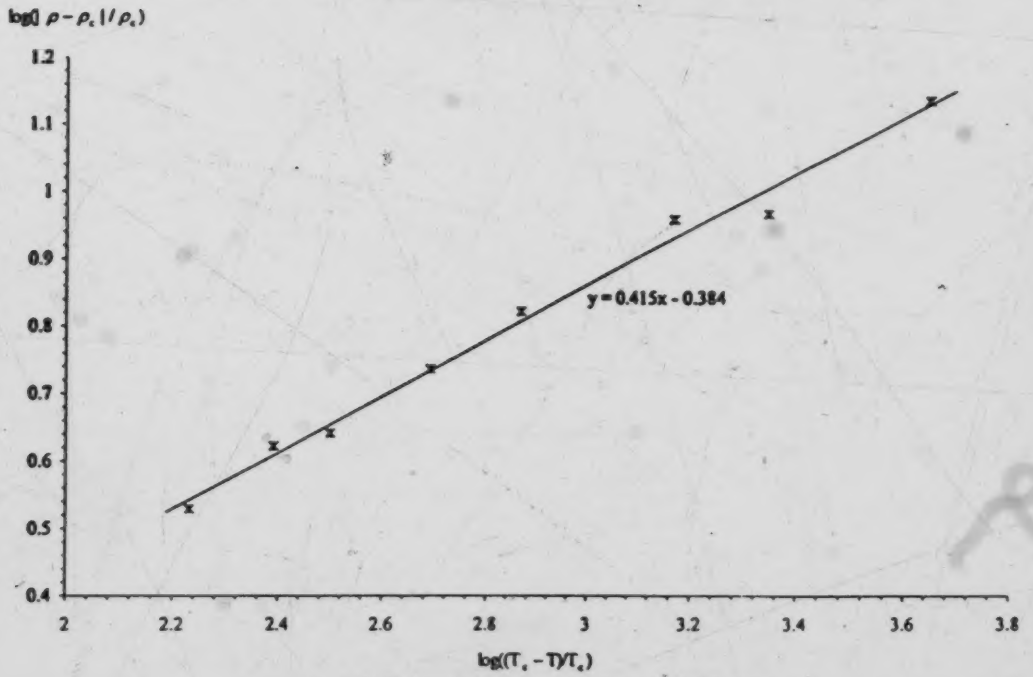

Fig. 3.12 Fitting the Coexistence Curve of Bulk Neon

It must also be pointed out that some care must be exercised in the interpretation of the results obtained for neon confined in aerogels. Although the neon pressure in the aerogel was expected to be the same as that in the bulk, the densities would certainly be different. This was because a few monolayers of neon atoms were expected to be tightly bound to the aerogel surfaces. Since aerogels have enormous surface area, we believed this would cause the density of confined neon to be higher than that of the bulk. The actual coexistence curve for confined neon was thus expected to shift slightly to the right. It would therefore be quite meaningless for us to make an attempt to curve-fit the current results since true exponents and amplitude fits would not be obtained.

Nonetheless, some definite conclusions can still be made. The critical temperature of confined neon is lower than that of the bulk by 0.04 K. Its coexistence curve is still fairly broad although it is shifted to the right with respect to the bulk curve. This is in good agreement with the predictions of the theoretical model discussed in sec. 1.5.3 but quite different from the results of Chan *et. al.* (sec. 1.5.2). If the chosen model is correct, then the broad plateau observed for the confined neon probably indicates that the interaction between the aerogel surfaces and the neon fluid is weaker than that between the neon atoms. In fact, this may be the likely cause for the difference between our results and that of Chan's group. Another point to note is that the curves obtained by Chan *et. al.* for confined fluids covered only a very limited range of density. It is thus quite possible for their curves to broaden significantly at lower temperatures.

3.6 Concluding Remarks

In this work, we have demonstrated that ultrasonics techniques may be employed to map out the coexistence curve of confined fluids. Although we have yet to achieve an understanding of the actual mechanisms at work, the velocity dips and attenuation peaks can still serve as effective markers of phase transitions. Difficulties surrounding the transmission of ultrasonic signals through aerogels of high porosity can now be overcome by growing the aerogels in glass capillary array samples so that more work can be done in understanding the effects of quenched disorder at very low concentrations. Perhaps the most obvious accomplishment shown in this work is that ultrasonic techniques can now be used in glass capillary array samples to study the bulk behavior of fluids.

Nevertheless, some improvements may still be made on our experimental techniques. For example, we may pot our samples in epoxy to eliminate the bulk neon lying outside. This will allow us to determine the actual neon density in the aerogels and so map out the true coexistence curve. With the latter, we can then investigate whether phase transitions in aerogels and bulk belong to the same universality class. Furthermore, such an improvement will serve to minimize the temperature and pressure fluctuations due to movement of neon gas between the capillary system and the large experimental cell. If a clearer interpretation of the ultrasonic velocities is desired, sloshing of the highly compressible fluids in the pores may be minimized or eliminated by using aerogels of higher density, GCA samples with smaller pores or lower sound frequencies. Simultaneous capacitive measurements of the neon density (see ref. [3.5]) in the aerogels can also be made to reduce the possibility of spurious effects due to, say capillary condensation. Of course, we may also try to work with other fluids, especially helium, the physicists' favorite element.

References

[1.1] E. Molz, A. P. Y. Wong, M. H. W. Chan, and J. R. Beamish, Phys. Rev. B **48**, 5741 (1993)

[1.2] A. P. Wong, and M. H. W. Chan, Phys. Rev. Lett. **65**, 2567 (1990)

[1.3] A. P. Wong, S. B. Kim, W. I. Goldburg, and M. H. W. Chan, Phys. Rev. Lett. **70**, 954 (1993)

[1.4] Z. Zhuang, A.G. Casielles, and D. S. Cannell, Phys. Rev. Lett. 77, 2969 (1996)

[1.5] E. B. Molz, and J. R. Beamish, J. Low Temp. Phys. **101**, 1055 (1995)

[1.6] S. B. Kim, J. Ma, and M. H. W. Chan, Phys. Rev. Lett. **71**, 2268 (1993); Physica B **197**, 249 (1994)

[1.7] A. G. Chynoweth, and W. G. Schneider, J. Chem. Phys. **20**, 1777 (1952)

[1.8] K. Kawasaki, in *Critical Phenomena*, edited by M. S. Green, Academic, New York, 1971

[1.9] W. F. Saam, and M. W. Cole, Phys. Rev. B **11**, 1086 (1975)

[1.10] D. D. Awschalom, J. Warnock, and M. W. Shafer, Phys. Rev. Lett. **57**, 1607 (1986)

[1.11] J. C. LeGuillou, and J. Zinn-Justin, Phys. Rev. Lett. **39**, 95 (1977), Phys. Rev. B **21**, 3976 (1976)

[1.12] A. Maritan, M. R. Swift, M. Cieplak, M. H. W. Chan, M. W. Cole, and J. R. Banavar, Phys. Rev. Lett. **67**, 1821 (1991)

[1.13] J. P. Donley, and A. J. Liu, Phys. Rev. E **55**, 539 (1997)

[1.14] H. Nakanishi, and M. E. Fisher, J. Chem. Phys. **78**, 3279 (1983)

[1.15] M. A. Biot, J. Acoust. Soc. Am. **28**, 168 (1956), J. Acoust. Soc. Am. **28**, 179 (1956)

[1.16] *Aerogels*, edited by J. Fricke, Springer-Verlag, New York, 1985

[1.17] C. W. Garland, in *Physical Acoustics*, edited by W. P Mason and R. N. Thurston, Academic, New York, 1970, Vol. 7

[1.18] *Adsorption, Surface Area and Porosity*, edited by S.J. Gregg and K. S. W. Sing, Academic, New York, 1982

[1.19] E. B. Molz, Ph.D. Thesis (unpublished), University of Alberta, 1995

[1.20] D. Fisher, G. M. Grinstein, and Anil Khurana, Physics Today **41**, No. 12, 56 (1988)

[1.21] E. D. Adams, Y. H. Tang, K. Uhlig, and G. E. Haas, J. Low Temp. Phys. **66**, 85 (1996)

[1.22] D. Sarid, and D. S. Cannell, Phys. Rev. A **15**, 735 (1977)

[1.23] M. E. Fisher, in *Critical Phenomena*, edited by F. J. W. Hahne, Springer-Verlag, Berlin, 1983

[2.1] *Elastic Waves in Solids*, E. Dieulesaint and D. Royer, John Wiley & Sons, New York, 1980

[2.2] Ying Xie, M.Sc. Thesis (unpublished), University of Alberta, 1995

[2.3] J. Gross, J. Fricke, and L. W. Hrubesh, J. Accoust. Soc. Am. **91**, 2004 (1992)

[2.4] A. Michels, T. Wassenaar, and P. Louwerse, Physica's Grav **26**, 539 (1960)

[2.5] S. Brunauer, P. H. Emmett, and E. Teller, J. Am. Chem. Soc. **60**, 309 (1938)

[2.6] M. J. Paetkau, Ph.D. Thesis (unpublished), University of Alberta, 1998

[2.7] K. L. Warner, and J. R. Beamish, J. Appl. Phys. **63**, 4372 (1988)

[3.1] H. L. Swinney, and D. L. Henry, Phys. Rev. A **8**, 2586 (1973)

[3.2] C. L. Yaws, J. R. Hopper, and M. G. Rojas, Chem. Eng. **82** (4), 87 (1975)

[3.3] M. H. W. Chan, Phys. Rev. B **21**, 1187 (1980)

[3.4] P. C. Hohenberg and M. Barmatz, Phys. Rev. A **6**, 289 (1972)

[3.5] M. W. Pestak, and M. H. W. Chan, Phys. Rev. B **30**, 274 (1984)

Appendix

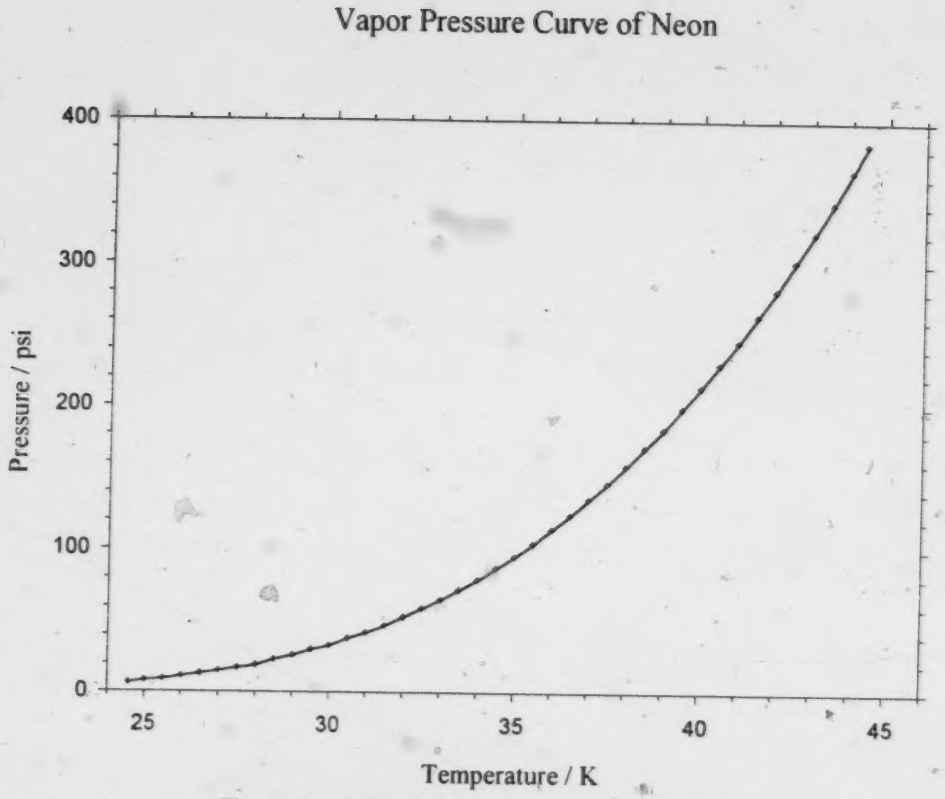

The triple and critical points of neon are normally given as (24.56 K, 6.3 psi) and (44.48 K, 394.5 psi) respectively.